



# Isomer sieving and the selective formation of terminal methyl isomers in reactions of linear alkanes on one-dimensional zeolites



Gina Noh<sup>a</sup>, Stacey I. Zones<sup>b</sup>, Enrique Iglesia<sup>a,\*</sup>

<sup>a</sup> Department of Chemical and Biomolecular Engineering, University of California at Berkeley, Berkeley, CA 94720, United States

<sup>b</sup> Chevron Energy Technology Company, Richmond, CA 94801, United States

## ARTICLE INFO

### Article history:

Received 20 March 2019

Revised 12 June 2019

Accepted 12 July 2019

### Keywords:

Isomerization

$\beta$ -scission

Bifunctional catalysis

Pore mouth catalysis

Zeolites

One-dimensional zeolites

## ABSTRACT

Diffusional hurdles enhance secondary interconversions of monomethyl isomers formed as primary products in bifunctional metal-acid isomerization of n-alkanes. One-dimensional medium-pore zeolites preferentially place methyl branches near the end of the isoalkane chains in what has been described as “pore mouth catalysis”; they also lead to low  $\beta$ -scission selectivities compared with three-dimensional frameworks similar in void size. n-Heptane and n-hexane reactions on acid forms of aluminosilicates of different channel size and connectivity (Al-MCM-41, FAU, SFH, BEA, MFI, MEL, SVR, TON, MTT; as mixtures with a Pt function) and crystallite size and proton density show that intracrystalline alkene concentration gradients are more consequential for larger and more branched molecules, as a result of their higher reactivity and lower diffusivity, and that the products form using all intracrystalline protons instead of only those near pore mouths. For both C<sub>6</sub> and C<sub>7</sub> reactants, 2-methyl to 3-methyl isoalkane ratios are those expected from equilibrium on large-pore zeolites (FAU, SFH, BEA). In contrast, these isomer ratios reflect the preferential sieving of the faster diffusing 2-methyl isomers from isoalkene products present as equilibrated mixtures within crystallites on medium-pore (10-MR) zeolites. These sieving effects are most evident for one-dimensional 10-MR frameworks because their void structures lead to stronger concentration gradients and more selective sieving of the faster diffusing isoalkenes. These effects are weaker on three-dimensional 10-MR structures because of less severe diffusional constraints, but the intersecting channels in these frameworks create local cage-like structures that favor  $\beta$ -scission through the preferential retention of dimethylpentenes, which act as the sole precursors to scission products. One-dimensional structures lack such channel undulations and cage-like intersections; as a result, one-dimensional medium-pore TON and MTT frameworks lead to low  $\beta$ -scission selectivities. This work demonstrates the essential, yet often overlooked, coupling between reactive and diffusive properties of zeolite materials in determining reactivity and selectivity in practice.

© 2019 Elsevier Inc. All rights reserved.

## 1. Introduction

Bifunctional isomerization reactions of linear alkanes selectively increase their skeletal branching, thus improving the low-temperature flow properties that make such molecules useful as precursors to fuels and lubricants [1,2]. These reactions involve kinetically-relevant acid catalysis of alkene intermediates that form locally at equilibrium concentrations on a separate dehydrogenation-hydrogenation metal function [3,4]. Turnover rates for primary isomerization events on protons present within voids and channels of molecular dimensions are influenced by the stabilization of intermediates and transition states through

van der Waals interactions [5]. The same voids and channels that confer catalytic diversity to zeolitic acids through confinement also impose diffusional hurdles that cause the selective retention of the more highly-branched molecules formed in isomerization events. These isomers also undergo more facile acid-catalyzed secondary isomerization and  $\beta$ -scission reactions than their less branched reactant counterparts, resulting in strong diffusional enhancements of such secondary reactions [5]. The intracrystalline concentration gradients imposed by these diffusional hurdles require reaction-transport formalisms [5–7] in order to extract from rate data the intrinsic reactivity and selectivity of confined protons, which are given by the products formed in single surface sojourns; these formalisms are used here to assess the contributions of intracrystalline secondary reactions, which influence the relative concentrations of isomers and  $\beta$ -scission products. These

\* Corresponding author.

E-mail address: [iglesia@berkeley.edu](mailto:iglesia@berkeley.edu) (E. Iglesia).

reaction-transport descriptions, taken together with experiments that allow monotonic increases in intracrystalline proton density (and thus in the contributions of diffusion-enhanced secondary reactions) by the desorption of pre-adsorbed  $\text{NH}_3$  titrants during catalysis, are able to assess intrinsic reactivities and selectivities for n-heptane [5] and 2,4-dimethylpentane [7] isomerization and  $\beta$ -scission on microporous solid acids.

The isomerization of n-alkanes catalyzed by one-dimensional zeolites (TON, MTT) and zeotypes (SAPO-11) in their respective acid forms favors the formation of single methyl branches while maintaining low  $\beta$ -scission selectivities, features that make them especially attractive to improve the flow properties of paraffinic streams for use as fuels and lubestocks. These methyl branches tend to be located preferentially near the end of alkane backbones, a feature often attributed to “pore-mouth” catalysis [8–11]. This heuristic picture envisions linear alkanes as entering one-dimensional channels only partially and then undergoing dehydrogenation and isomerization events in the parts of the molecule that can access these protons near pore mouths [8–11].

This study demonstrates the kinetic relevance of all intrapore protons (instead of only those near pore mouths) and how secondary reactions, enhanced by intracrystalline concentration gradients of isomer products, lead to the preferential sieving of isomers with single methyl branches near the end of their backbones. Such specificity merely reflects the faster diffusion of such molecules relative to the other skeletal isomers formed and the ubiquitous presence of severe intracrystalline gradients for all isomers. These effects are most clearly evident in one-dimensional (1-D) 10-membered ring (MR) zeolites, merely because they impose greater diffusional hurdles than the larger or more connected voids present in other zeotypes [12–14]. The absence of channel intersections in these one-dimensional networks avoids undulations along diffusion paths, thus preventing the formation and retention (caused by their highly-inhibited local transport) of the highly-branched isomers that act as the sole precursors to  $\beta$ -scission products; such undulation effects were previously shown to enhance secondary reactions in 2,4-dimethylpentane isomerization and  $\beta$ -scission [7], as well as the secondary  $\beta$ -scission of alkene oligomerization products [15]. The results shown provide compelling evidence against any detectable role of “pore-mouth” catalysis in determining the number and location of methyl branches along isomer backbones or in the avoidance of secondary  $\beta$ -scission events.

Mechanistic interpretations of reactivity and selectivity for isomerization reactions catalyzed by protons within mesoporous aluminosilicates, large-pore zeolites, and three-dimensional zeolites

(Al-MCM-41, FAU, SFH, BEA, MEL, MFI, SVR) and also within one-dimensional zeolites (MTT and TON) (each as physical mixtures with a Pt/SiO<sub>2</sub> dehydrogenation function) are combined here with experiments that probe the effects of proton density and crystallite dimensions on measured isomerization rate constants, as well as on the relative rates of isomerization and of secondary skeletal rearrangements and  $\beta$ -scission for n-hexane and n-heptane reactants. These physical mixtures allow the precise definition of the “acid domain” as the aluminosilicate crystallites, thus allowing accurate assessments of diffusional effects using the required reaction-transport formalisms, as well as the unequivocal demonstration that all intrapore protons, instead of those only near the pore mouths, mediate these catalytic turnovers.

Intracrystalline gradients of reactant-derived isoalkenes favor their interconversions, and ultimately their equilibration, within a given acid domain before they reach the extracrystalline hydrogenation function. Such phenomena are demonstrated here through quantitative assessments of the effects of these gradients on the rates of primary and secondary reactions of n-hexane and n-heptane during the desorption of  $\text{NH}_3$  titrants pre-adsorbed at intracrystalline Brønsted acid sites. These data and their mechanistic interpretations show that observations previously attributed to pore-mouth effects merely reflect the preferential sieving of isoalkenes that undergo rapid interconversions within highly constrained void structures that impose strong diffusional hurdles but that lack the framework undulations that enhance  $\beta$ -scission selectivities. In doing so, this study illustrates how the inherent complexity and the inextricable links between the diffusive and confining properties of void structures lead to their unique reactivity and selectivity in practice.

## 2. Methods and materials

### 2.1. Catalyst synthesis and characterization

Mesoporous and microporous aluminosilicates (Table 1) were obtained from commercial sources (Al-MCM-41: Sigma-Aldrich; MFI, BEA: Zeolyst), synthesized according to reported protocols (MTT-1, SFH [16]; FAU [17]; MEL, SVR [7]; TON-1, MTT-3 [18]; MTT-2 [19]), or prepared using procedures described below (TON-2).

TON-2 was prepared by combining *N,N*-dimethylimidazolium hydroxide (synthesized as previously reported [18], 1 M, 14 mmol),  $\text{Al}_2(\text{SO}_4)_3 \cdot 18\text{H}_2\text{O}$  (51.4% wt.  $\text{Al}_2(\text{SO}_4)_3$ , Mallinckrodt Chemical, 1 mmol), sodium silicate (9% wt.  $\text{Na}_2\text{O}$ , 28% wt.  $\text{SiO}_2$ ,

**Table 1**  
Mesoporous and microporous aluminosilicate solid acids.

Solid acid	Source	Si/Al <sup>a</sup>	H <sup>+</sup> /Al	R <sup>2</sup> /D <sub>nr</sub> /s <sup>b</sup>
Al-MCM-41	Sigma-Aldrich	37.8	0.36 <sup>c</sup>	–
FAU	[17]	7.5	0.39 <sup>c</sup>	–
SFH <sup>*</sup>	[16]	45.0	0.71 <sup>d</sup>	–
BEA	Zeolyst	11.8	0.27 <sup>c</sup>	–
MEL	[7]	20.6	0.75 <sup>d</sup>	–
MFI	Zeolyst	29.2	0.64 <sup>d</sup>	–
SVR	[7]	20.2	0.20 <sup>d</sup>	–
TON-1 <sup>*</sup>	[18]	39.6	0.68 <sup>d</sup>	528 (±21)
TON-2 <sup>*</sup>	This work	43.1	0.36 <sup>d</sup>	153 (±46)
MTT-1 <sup>*</sup>	[16]	16.6	0.46 <sup>d</sup>	228 (±37)
MTT-2 <sup>*</sup>	[19]	34.1	1.07 <sup>d</sup>	25.2 (±3.4)
MTT-3 <sup>*</sup>	[18]	73.0	0.82 <sup>d</sup>	298 (±15)

<sup>\*</sup> one-dimensional zeolite frameworks.

<sup>a</sup> elemental analysis ICP-OES (Galbraith Laboratories).

<sup>b</sup> characteristic diffusion times measured from transient uptake of n-pentane at 423 K (Section 2.1).

<sup>c</sup> proton counts from 2,6-di-*tert*-butylpyridine titration during n-heptane isomerization at 548 K [5].

<sup>d</sup> proton counts from  $\text{NH}_3$  evolved during rapid heating of  $\text{NH}_4^+$ -zeolites.

Fisher, 100 mmol), and deionized water (32 g). Sulfuric acid (95–98% wt, Fisher, 2.5 g) was then added to this mixture, which was then placed into Teflon liners held within an autoclave (Parr, 23 cm<sup>3</sup>; 43/60 Hz) at 433 K for 120 h.

The solids formed were collected by filtration, rinsed with deionized water (until the filtrate conductivity was <50 S m<sup>-1</sup>), and allowed to stand at ambient temperature for 12 h. All synthesized and as-received solids were treated in air (2.5 cm<sup>3</sup> g<sup>-1</sup> s<sup>-1</sup>; extra dry, Praxair) at 823 K (0.0167 K s<sup>-1</sup>) for 4 h and exchanged with NH<sub>4</sub>NO<sub>3</sub> three times by contacting with 0.1 M NH<sub>4</sub>NO<sub>3</sub> (>98%, Sigma-Aldrich; 300 g-solution [g-zeolite]<sup>-1</sup>; 298 K) to obtain their respective NH<sub>4</sub><sup>+</sup>-exchanged forms. After the final exchange with NH<sub>4</sub>NO<sub>3</sub>, the solids were filtered and washed with deionized water (resistivity > 17.6 Ω cm<sup>-2</sup>; 1500 g [g zeolite]<sup>-1</sup>).

Si and Al contents were determined by inductively-coupled plasma optical emission spectroscopy (ICP-OES, Galbraith Laboratories). Brønsted acid site densities in Al-MCM-41 and FAU were measured from the number 2,6-di-*tert*-butylpyridine titrants required to fully suppress n-heptane isomerization reactions [5]. These hindered amines are selective for protons because steric hindrance prevents their coordination to Lewis acid centers; they cannot, however, access protons within medium-pore or one-dimensional large-pore zeolites [16] (MFI, SFH, TON, MTT). Protons were counted on such zeolites by measuring the number of NH<sub>3</sub> molecules evolved during rapid heating of their respective NH<sub>4</sub><sup>+</sup>-exchanged forms [5].

The characteristic diffusion times for n-pentane ( $R^2/D_{np}$ , units: s;  $R$  is zeolite crystallite radius,  $D_{np}$  is diffusivity of n-pentane; nP; > 98%, Sigma-Aldrich; purified by three freeze-pump-thaw cycles) were measured for each one-dimensional zeolite (TON, MTT) at 423 K using experimental and mathematical analysis protocols previously reported for transient uptakes of 2,2-dimethylbutane (22DMB) [5]. These  $R^2/D_{np}$  values for TON and MTT and Si and Al contents and H<sup>+</sup> counts for each aluminosilicate are reported in Table 1.

The Pt/SiO<sub>2</sub> co-catalyst was synthesized as previously described [5] and its metal dispersion (88%) was determined from total H<sub>2</sub> uptakes at 373 K, assuming a 1:1 H:Pt<sub>s</sub> stoichiometry (where Pt<sub>s</sub> is the number of Pt surface atoms). Intrapellet physical mixtures of Pt/SiO<sub>2</sub> with each aluminosilicate were prepared by combining the metal and acid functions, which were separately crushed and sieved to ensure that all monofunctional aggregates were smaller than 100 μm. Pt/SiO<sub>2</sub> and the aluminosilicate were then thoroughly combined using a mortar and pestle, pressed into wafers (Carver Bench Top Manual Press, 55 MPa), and crushed and sieved to retain aggregates 125–180 μm in size. The ratios of the individual functions for each intrapellet physical mixture were sufficient to maintain alkane-alkene dehydrogenation equilibrium during n-heptane isomerization (Pt<sub>s</sub>/H<sup>+</sup> > 7.8 [5], where Pt<sub>s</sub> was obtained from H<sub>2</sub> chemisorption and H<sup>+</sup> was determined as specified in Table 1). Such Pt<sub>s</sub>/H<sup>+</sup> ratios are also sufficient to equilibrate hexane-hexene interconversion at the extracrystalline dehydrogenation function, because n-hexane consumption rates are lower than those for n-heptane (Section 3.1) but their alkane-alkene interconversions on Pt are similar. Physical mixtures are denoted by their acid function (e.g., “MTT-1” for physical mixtures of Pt/SiO<sub>2</sub> and MTT-1).

## 2.2. Alkane isomerization and β-scission rate measurements

n-Hexane (nC<sub>6</sub>; >99.0%, Fluka; used as received) and n-heptane (nC<sub>7</sub>; > 99.5%, Acros Organics; used as received) isomerization and β-scission rates were measured at 548 K on all catalysts (0.10–0.20 g) using a tubular reactor (316 S.S., 12 mm i.d.) with plug-flow hydrodynamics. The bed temperature was measured using a K-type thermocouple placed within a thermowell aligned axially and positioned at the midpoint of the catalyst bed. Temperatures

were maintained using a three-zone resistively-heated furnace (Applied Test Systems Series 3210) with independent electronic controllers (Watlow, EZ-ZONE PM Series). Samples were treated in 10% H<sub>2</sub>/He mixtures (0.83 cm<sup>3</sup> s<sup>-1</sup>; 99.999% Praxair H<sub>2</sub>; 99.999% Praxair He) at 573 K (0.083 K s<sup>-1</sup>) for 2 h and then cooled to reaction temperature before catalytic measurements.

Liquid nC<sub>6</sub> or nC<sub>7</sub> reactants were introduced into mixed flowing streams of H<sub>2</sub> (99.999% Praxair H<sub>2</sub>) and He (99.999% Praxair He) using a syringe pump (Cole-Parmer 780200C Series) through an injection port maintained above 423 K. Transfer lines after the point of liquid introduction were kept above 423 K in order to prevent reactant or product condensation. H<sub>2</sub>, He, and reactant alkane pressures were varied independently to set alkane/H<sub>2</sub> molar ratios (0.003–0.15) at the reactor inlet and to maintain differential reactant conversions (<8%). Reactant and product concentrations in the reactor effluent were measured using on-line gas chromatography (Agilent 6890N; Agilent HP-1 column 50 m × 0.32 mm × 1.05 μm) and flame ionization detection.

Measured rates are reported on a per H<sup>+</sup> basis, with the number of H<sup>+</sup> determined as described in Section 2.1 (Table 1). Approach to equilibrium values were determined for isomerization ( $\eta_{j,i}$  for species  $i$  to species  $j$ ):

$$\eta_{j,i} = \left(\frac{P_j}{P_i}\right) K_{j,i}^{-1} \quad (1)$$

where  $P_i$  and  $P_j$  are the pressures of species  $i$  and  $j$  (in bar), and  $K_{j,i}$  is the  $j$ - $i$  equilibrium constant at 548 K, determined from tabulated thermodynamic data at 1 bar standard state [20], and for β-scission ( $\eta_{\beta,nC_7}$  for nC<sub>7</sub> to C<sub>3</sub> and C<sub>4</sub> products; nC<sub>6</sub> β-scission products were below detection limits):

$$\eta_{\beta,nC_7} = \left(\frac{P_{C_3} P_{C_4}}{P_{nC_7}}\right) K_{\beta,nC_7}^{-1} \quad (2)$$

where  $P_{C_3}$  and  $P_{C_4}$  are the pressures (in bar) of C<sub>3</sub> and C<sub>4</sub> β-scission products, respectively, and  $K_{\beta,nC_7}$  is the equilibrium constant for β-scission reactions of nC<sub>7</sub> at 548 K, obtained from tabulated thermodynamic data [20]. Measured rates ( $r_{net}$ ) were corrected for approach to equilibrium to obtain forward rates ( $r_{forward}$ ):

$$r_{forward} = r_{net} \left(1 - \eta_{prod,react}\right)^{-1} \quad (3)$$

Measured β-scission products remained far from equilibrium at all conditions ( $\eta_{\beta,nC_7} < 10^{-4}$ ), rendering the effects of such corrections negligible.

## 2.3. Alkane isomerization and β-scission selectivity measurements during desorption of weakly-bound NH<sub>3</sub> titrants

Isomerization rates, product formation rate ratios, and product selectivities for n-hexane and n-heptane reactions were measured using mixtures of the two reactants as pre-adsorbed NH<sub>3</sub> titrants desorbed, a process that gradually increases intracrystalline proton densities. These methods were used to determine single-sojourn selectivities and contributions from diffusion-enhanced secondary reactions in n-heptane isomerization and 2,4-dimethylpentane isomerization and β-scission reactions [5,7]. Here, these methods are used to assess the presence and severity of intracrystalline reactant alkene concentration gradients in zeolite materials (Section 3.1.2) and the contributions from diffusion-enhanced secondary reactions on product selectivities (Section 3.2) by systematically increasing the volumetric productivity of zeolite crystallites as the titrant desorbs.

Samples were treated as described in Section 2.2, and rates and selectivities were measured before exposure to NH<sub>3</sub> titrants (100 kPa H<sub>2</sub>, H<sub>2</sub>/nC<sub>7</sub> ~200, H<sub>2</sub>/nC<sub>6</sub> ~200, 573 K). Samples were

exposed to a stream of NH<sub>3</sub> and He (0.83 cm<sup>3</sup> s<sup>-1</sup>, 1% NH<sub>3</sub> in He, Praxair; 99.999%, Praxair He) for 2 h at 573 K. Rates and selectivities were measured (100 kPa H<sub>2</sub>, H<sub>2</sub>/nC<sub>7</sub> ~200, H<sub>2</sub>/nC<sub>6</sub> ~200) as NH<sub>3</sub> titrants desorbed gradually from protons and reaction rates concurrently increased, ultimately returning to within 90% of their initial values within 5 h.

The fraction of the steady-state rates of nC<sub>6</sub> isomerization ( $\chi(t)$ ) measured at each time  $t$  during NH<sub>3</sub> desorption is defined as:

$$\chi(t) = \frac{r_{nC_6}(t)}{r_{nC_6}} \quad (4)$$

where  $r_{nC_6}(t)$  is the nC<sub>6</sub> isomerization rate at a given time during NH<sub>3</sub> desorption and  $r_{nC_6}$  is the nC<sub>6</sub> isomerization rate at steady state. In the absence of concentration gradients of reactant alkenes,  $\chi(t)$  is strictly proportional to  $\rho_{H^+}$  (the volumetric density of protons). When rates are influenced by reactant alkene concentration gradients, such concentration gradients become more severe as  $\rho_{H^+}$  (and  $\chi(t)$ ) increase with time and as the number of NH<sub>3</sub> titrants desorbed; rates in this limit depend on  $\rho_{H^+}^2$ . As a result,  $\chi(t)$  remains a directional indicator of  $\rho_{H^+}$  values for such samples, but these two quantities are no longer strictly proportional to each other.

Fractional selectivities ( $S_{\text{react,prod}}$ ) are reported here on a carbon basis and defined as:

$$S_{\text{react,prod}} = \frac{r_{\text{react,prod}}}{\sum_{\text{prod}} r_{\text{react,prod}}} \quad (5)$$

where  $r_{\text{react,prod}}$  is the measured formation rate of each product (prod) from reactant (react). Intrinsic fractional selectivities ( $S_{\text{react,prod,0}}$ ) are defined as:

$$S_{\text{react,prod,0}} = \frac{r_{\text{react,prod,0}}}{\sum_{\text{prod}} r_{\text{react,prod,0}}} \quad (6)$$

where the subscript "0" denotes product formation rates resulting from single sojourn reaction events. Such values are expected to become accessible by extrapolation of measured selectivities to zero  $\chi(t)$  values during titrant desorption, because these conditions lead to weak intracrystalline gradients that do not influence the measured reactivity or selectivity.

### 3. Results and discussion

#### 3.1. n-Heptane and n-hexane isomerization reactions: Intracrystalline concentration gradients of reactant-derived linear alkenes and consequences for isomerization turnover rates

n-Hexane (nC<sub>6</sub>) and n-heptane (nC<sub>7</sub>) isomerization and  $\beta$ -scission rates and selectivities were measured on mesoporous aluminosilicates (Al-MCM-41), three-dimensional zeolites (FAU, BEA, MEL, MFI, SVR), and one-dimensional zeolites (SFH, TON, MTT). These solid acids were used as physical mixtures with sufficient amounts of Pt/SiO<sub>2</sub> co-catalysts to ensure alkane-alkene equilibration in the fluid phase surrounding the acid domains ( $P_t/H^+ > 7.8$  [5]; Section 2.1). Isomerization rates of n-hexane were lower (Fig. 1) than isomerization rates of n-heptane because the lower proton affinity of smaller alkenes leads to less stable carbocations at the kinetically-relevant ion-pair isomerization transition states [21]. Thus, the  $P_t/H^+$  ratios sufficient to achieve such equilibration for n-heptane reactants are also able to do so for n-hexane reactants. The equilibrated alkene regioisomers formed (on the Pt function) from each alkane with a given backbone are denoted here by the superscript "=" (e.g., nC<sub>6</sub><sup>=</sup>, nC<sub>7</sub><sup>=</sup> for linear alkenes) and treated as a single chemical species in the kinetic treatments that follow, unless explicitly noted otherwise.

The reaction network and the primary or secondary nature of the reactions that occur during isomerization and  $\beta$ -scission of

nC<sub>6</sub> and nC<sub>7</sub> reactants are depicted in Schemes 1a and b, respectively, with only the saturated analogs of each isomer shown for visual clarity. Linear heptene isomers directly form 2-methylhexenes (2MH<sup>=</sup>) and 3-methylhexenes (3MH<sup>=</sup>), which interconvert via facile methyl shifts (Section 3.2). These methylhexenes undergo subsequent isomerization reactions to form dimethylpentenes (2,3; 2,4; 2,2; and 3,3), which also interconvert through methyl and hydride shifts and ultimately act as the precursors required for all  $\beta$ -scission products detected (propene and isobutene) [5].

Similarly, linear hexenes form 2-methyl (2MP<sup>=</sup>) and 3-methylpentenes (3MP<sup>=</sup>), which interconvert rapidly and can undergo subsequent isomerization to form 2,3-dimethylbutenes. 2,2-Dimethylbutenes, detected only on FAU and in trace amounts (<0.0005 fractional selectivity), form only via secondary methyl-shifts of 2,3-dimethylbutenes [22]; they are lumped here with their 2,3-dimethylbutene precursors.  $\beta$ -Scission products were not detected during n-hexane reactions on any of the solid acids. 2,3-, 2,2-, and 3,3-Dimethylpentenes from nC<sub>7</sub> reactants were detected only on FAU and in trace amounts (<0.0005 fractional selectivity); all dimethylpentene isomers are lumped together because the formation of 2,2- and 3,3-dimethylpentene products both require the initial formation of 2,3-dimethylpentene [5].

For both n-alkane reactants, all detected products form via the initial conversion of linear alkenes to their monomethyl isomers, which then undergo secondary isomerization (and also  $\beta$ -scission in the case of nC<sub>7</sub> reactants). Consequently, measured reactant conversion turnover rates solely reflect the rates of the initial isomerization events that form 2MH and 3MH (for nC<sub>7</sub>) and 2MP and 3MP (for nC<sub>6</sub>) and are therefore denoted here as isomerization turnover rates.

n-Hexane and n-heptane isomerization turnover rates on MTT and TON with different crystallite sizes and volumetric proton densities are reported next. These data are described using reaction-transport formalisms that detect the presence of and the consequences of intracrystalline concentration gradients of alkene reactants and products, which become particularly evident for medium-pore one-dimensional aluminosilicates.

#### 3.1.1. The role of intrapore protons in n-alkane isomerization reactions on MTT and TON

Fig. 1a shows n-hexane isomerization turnover rates (per H<sup>+</sup>) as a function of nC<sub>6</sub>/H<sub>2</sub> molar ratios on physical mixtures of Pt/SiO<sub>2</sub> with MTT or TON; these reactant molar ratios act as accurate surrogates for the equilibrium concentration of the linear hexene regioisomers that form at the extracrystalline Pt function. These zeolites consist of one-dimensional channels with similar confining environments for the active protons (maximum diameter of a sphere that can be included, which we refer to as the diameter of the largest contained sphere ~0.51 nm [23]). Fig. 1b shows the corresponding isomerization turnover rates for n-heptane reactants. Isomerization rates depend linearly on these molar ratios for both n-alkanes, but gradually approach constant values as molar ratios (and linear alkene concentrations) increase. Such trends are accurately described by a rate expression with the functional form:

$$\frac{r_{\text{isom,n}}}{[H^+]} = \frac{k_{1,n}K_{\text{dehyd,n}}\left(\frac{P_n}{P_{H_2}}\right)}{1 + \frac{k_{1,n}K_{\text{dehyd,n}}}{k_{0,n}}\left(\frac{P_n}{P_{H_2}}\right)} \quad (7)$$

Here, n represents the n-alkane reactant (i.e., nC<sub>6</sub> and nC<sub>7</sub>),  $K_{\text{dehyd,n}}$  is the equilibrium constant for the dehydrogenation of each n-alkane to all n-alkene regioisomers ( $K_{\text{dehyd,nC}_6} = 17.6$  Pa,  $K_{\text{dehyd,nC}_7} = 19.8$  Pa at 548 K [20,24]), and  $k_{1,n}$  and  $k_{0,n}$  are the first-order and zero-order rate constants for isomerization of each n-alkane.

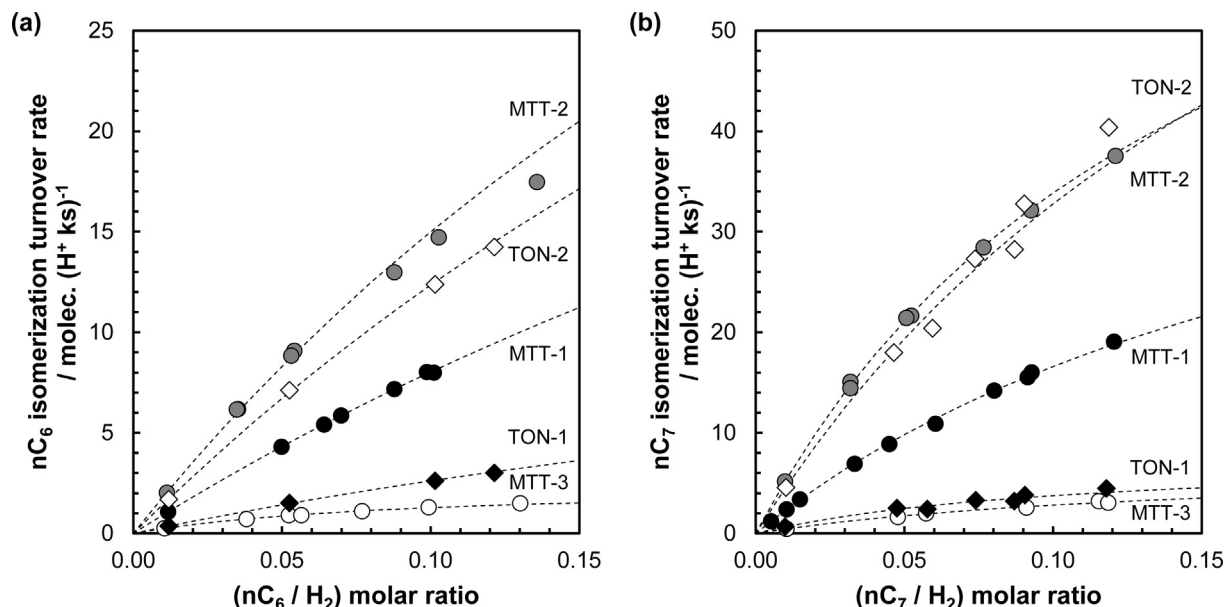
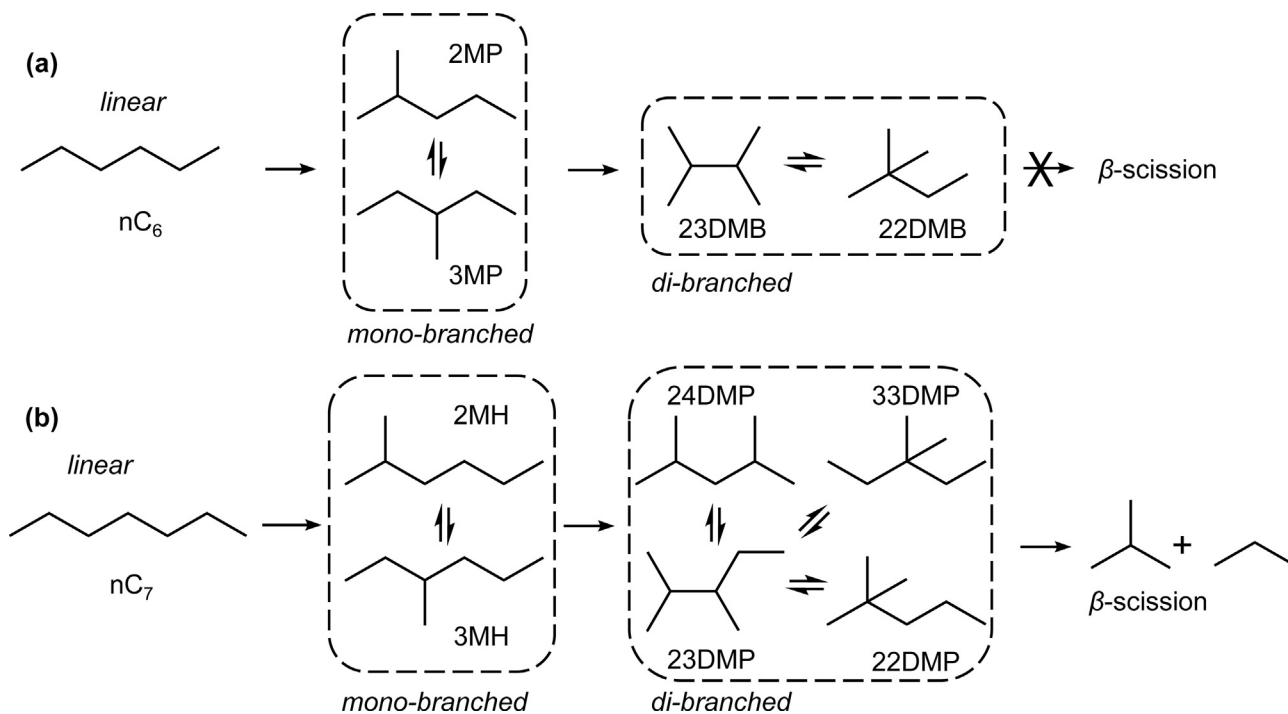


**Fig. 1.** (a) n-Hexane isomerization turnover rates (per  $H^+$ ) as a function of  $(nC_6/H_2)$  molar ratio and (b) n-heptane isomerization turnover rates as a function of  $(nC_7/H_2)$  molar ratio on physical mixtures of  $Pt/SiO_2$  and MTT (circles; Table 1) or TON (diamonds; Table 1) (60–100 kPa  $H_2$ , 548 K); (alkane/ $H_2$ ) molar ratios are a surrogate for the equilibrium alkene concentration in the extracrystalline fluid phase. Dashed lines represent the regression of these data to the form of Eq. (9.1).



**Scheme 1.** Reaction pathways in (a) n-hexane and (b) n-heptane isomerization, shown for saturated products. Dashed boxes around isomers with the same degree of branching indicate rapid interconversion. The cross through the arrow indicates that products of the pathway are not detected.

This rate equation reflects elementary steps that transfer a proton from the aluminosilicate framework to the equilibrated pool of linear alkenes to form a pool of equilibrated alkoxides with the skeletal backbone of their respective alkenes and with all possible surface attachment points; they ultimately convert to alkoxides with product skeletal backbones in the sole kinetically-relevant step. Eq. (7) rigorously describes rate data in the absence of intracrystalline gradients because in such cases the alkene concentrations in the extracrystalline fluid phase (and used in Eq. (7)) are

the same as those in contact with all protons within zeolite crystallites. Small reactant molar ratios correspond to low concentrations of reactant-derived alkene regioisomers, which lead, in turn, to low alkoxide coverages and to rates proportional to these reactant ratios; these ratios are proportional to the linear alkene concentrations present in the extracrystalline fluid phase. As (alkane/ $H_2$ ) ratios increase, alkoxides become the most abundant surface intermediates (MASI), leading to rates that become independent of the prevalent alkene concentrations and reactant ratios [5,7,22].

Isomerization turnover rates for nC<sub>6</sub> (Fig. 1a) and nC<sub>7</sub> (Fig. 1b) in the first-order kinetic regime vary about ten-fold among different MTT samples. These MTT samples contain acid sites of similar strength [25,26], which reside within the same confining environment. Consequently, they should exhibit similar intrinsic reactivity (per H<sup>+</sup>) for each given reactant. These samples differ, however, in their volumetric density of protons ( $\rho_{H^+}$ ) and in their characteristic diffusion times ( $R^2/D_{np}$ ) (Table 1), both of which would influence the severity of any prevalent intracrystalline gradients and thus their consequences for reactivity and selectivity. A similar difference in rates ( $\sim 10$ -fold) is evident for the two TON zeolites used (Fig. 1), which also differ about two-fold in volumetric proton density and five-fold in characteristic diffusion times ( $R^2/D_{np}$ ; Table 1).

These differences in reactivity for sites similar in strength and present within the same confining environment reflect the kinetic consequences of intracrystalline gradients of reactant-derived alkenes. Intracrystalline concentration gradients depend on a Thiele modulus ( $\phi_n$ , for molecule  $n$ ) [27,28], given for a first-order reaction by:

$$\phi_n = \sqrt{\frac{k_{1,n}R^2\rho_{H^+}}{D_n}} \quad (8.1)$$

where  $k_{1,n}$  and  $D_n$  are the first-order rate constant and the molecular diffusivity of molecule  $n$ . Small  $\phi_n$  values ( $\leq 1$ ) lead to negligible gradients of molecule  $n$  and to measured turnover rates of strict chemical origins. Large  $\phi_n$  values ( $> 1$ ) lead to kinetically-consequential intracrystalline gradients and to rates that are influenced by the density of protons and the characteristic diffusion distance in each sample.

For a kinetic rate expression with the form of Eq. (7), a generalized Thiele modulus [29] ( $\Phi_n$ ) can be used to rigorously account for the effects of these reactant alkene concentration gradients on measured rates:

$$\Phi_n = \sqrt{\frac{k_{1,n}R^2\rho_{H^+}}{D_n} \frac{k_{1,n}K_{dehyd,n}\left(\frac{P_n}{P_{H_2}}\right)}{1 + \frac{k_{1,n}K_{dehyd,n}\left(\frac{P_n}{P_{H_2}}\right)}{k_{0,n}}}} \left( \frac{k_{1,n}K_{dehyd,n}\left(\frac{P_n}{P_{H_2}}\right)}{k_{0,n}} \right) - \ln \left( 1 + \frac{k_{1,n}K_{dehyd,n}\left(\frac{P_n}{P_{H_2}}\right)}{k_{0,n}} \right) \quad (8.2)$$

In the limit of  $\frac{k_{1,n}K_{dehyd,n}\left(\frac{P_n}{P_{H_2}}\right)}{k_{0,n}} \ll 1$ , where Eq. (7) reduces to an expression that is linear in the reactant molar ratios, the  $\Phi_n$  term (Eq. (8.2)) becomes equal to  $\phi_n$  (Eq. (8.1)).

The ratio of measured to intrinsic kinetic rates (or rate constants) is given by an effectiveness factor ( $\Gamma_n$  for species  $n$ ):

$$\Gamma_n = \frac{3}{\Phi_n^2} (\Phi_n \coth(\Phi_n) - 1) \frac{k_{1,n}K_{dehyd,n}\left(\frac{P_n}{P_{H_2}}\right)}{1 + \frac{k_{1,n}K_{dehyd,n}\left(\frac{P_n}{P_{H_2}}\right)}{k_{0,n}}} \quad (9.1)$$

which simplifies to the effectiveness factor for a first-order reaction [27,28] ( $\gamma_n$  for species  $n$ ):

$$\gamma_n = \frac{k_{1,n}^*}{k_{1,n}} = \frac{3}{\phi_n^2} (\phi_n \coth(\phi_n) - 1) \quad (9.2)$$

when  $\frac{k_{1,n}K_{dehyd,n}\left(\frac{P_n}{P_{H_2}}\right)}{k_{0,n}} \ll 1$ ; here,  $k_{1,n}^*$  and  $k_{1,n}$  are the measured and intrinsic rate constants, respectively. Eqs. (9.1) and (9.2) indicate that  $\Gamma_n$  (and  $\gamma_n$ ) values approach unity for small values of  $\Phi_n$  (and  $\phi_n$ ) and decrease inversely with  $\Phi_n$  ( $\Gamma_n = \Phi_n^{-1}$ ) for large  $\Phi_n$  values.

Measured rates can be regressed to the functional form of Eq. (9.1) to give the measured first-order rate constants ( $k_{1,n}^*$ ), which depend on the Thiele moduli for each reactant ( $\Phi_{nC_6}$  and  $\Phi_{nC_7}$ , Eq. (8.2)). The values of  $k_{1,nC_6}^*$  and  $k_{1,nC_7}^*$  obtained by regression of the data in Fig. 1 to the functional form of Eq. (9.1) are shown in

Fig. 2a and b as a function of a simplified form of the Thiele modulus (Eq. (8.1) and (8.2)).

The similar acid strength of aluminosilicates, irrespective of framework [25], and the similar confining environment for each framework type lead to transition states that must be stabilized to the same extent by the conjugate anion and by the van der Waals interactions imposed by each type of void structure. Consequently, intrinsic reactivities ( $k_{1,n}$ ) are expected to be similar for protons residing within any given aluminosilicate framework. The similar void structures of MTT and TON also lead to similar diffusivities for each given isomer in these two frameworks ( $D_n$  for species  $n$ ). Thus, only differences in proton density ( $\rho_{H^+}$ ) and acid domain size ( $R$ ) determine the severity of intracrystalline gradients prevalent in these zeolite frameworks.

The relevant domain size ( $R$ ) in Eqs. (8.1) and (8.2) is given by the zeolite crystallite radius, because the voids among zeolite crystallites in the aggregates of bifunctional mixtures are much larger than those within zeolite crystallites [30]. The radii of zeolite crystallites cannot be accurately determined from micrographs because crystallites are irregular in shape and distributed in size. Moreover, the size of such crystallites may not represent the relevant diffusion distances when barriers to transport are imposed by crystal defects (e.g., twinning and intergrowths [31]), the presence of polymorphs for some frameworks, or surface barriers. Instead, diffusion timescales ( $R^2/D_{np}$ ; measured using the transient uptakes of n-pentane for MTT and TON; details in Section 2.1) for n-pentane are used here as an accurate proxy for the relative ( $R^2/D_n$ ) values among samples with each given void environment. The defining equation for the Thiele modulus (Eq. (8.1)) for samples with a given framework is described by a simplified form of the Thiele modulus ( $\Xi$ ):

$$\Xi = \sqrt{\frac{R^2\rho_{H^+}}{D_{np}}} \quad (10)$$

as the relevant descriptor of intracrystalline concentration gradients of reactant alkenes for any one given framework.

The first-order rate constants for nC<sub>6</sub> (Fig. 2a) and nC<sub>7</sub> (Fig. 2b) isomerization on MTT and TON samples decreased with increasing  $\Xi$  values, as expected from reactant concentration gradients that become more consequential as proton densities and characteristic diffusion times increase for any given framework. These trends, considered alone, cannot preclude the exclusive some involvement by protons at external surfaces or near pore mouths, in which case, rate constants (per H<sup>+</sup>) would depend on  $\rho_{H^+}R$ , for uniformly distributed protons within quasi-spherical crystallites:

$$k_{1,n}^* = \frac{k_{1,n}}{\rho_{H^+}} \frac{4\pi R^2}{4\pi R^3/3} = \frac{k_{1,n}}{\rho_{H^+}} \frac{3}{R} \quad (11)$$

Such a single-valued dependence of  $k_{1,n}^*$  on  $\rho_{H^+}R$  would resemble that expected from a dependence on  $\Xi^2$  ( $\rho_{H^+}R^2/D_{np}$ ; Eq. (10)) and render it difficult to distinguish the two plausible causes for modest changes in  $\rho_{H^+}$  or  $R$ .

The sole involvement of fully accessible external sites, however, would cause reactants that differ in reactivity and diffusivity to depend similarly on proton density ( $\rho_{H^+}$ ) and diffusion timescales ( $R^2/D_{np}$ ). When all intrapore protons are involved in isomerization events, the ratio of measured rate constants for nC<sub>7</sub> and nC<sub>6</sub> ( $k_{1,nC_7}^*/k_{1,nC_6}^*$ ) would decrease as  $\rho_{H^+}$  or  $R^2/D_{np}$  increase, given that nC<sub>6</sub> and nC<sub>7</sub> rates are both not in the same extreme asymptotic regime of Eq. (9) ( $\phi_n \gg 1$  or  $\ll 1$ ); these decreases in measured rate constant ratios as  $\Xi^2$  increases would reflect the more severe concentration gradients of the nC<sub>7</sub> reactants as a result of their slower diffusion and greater reactivity, compared with their smaller analogs.

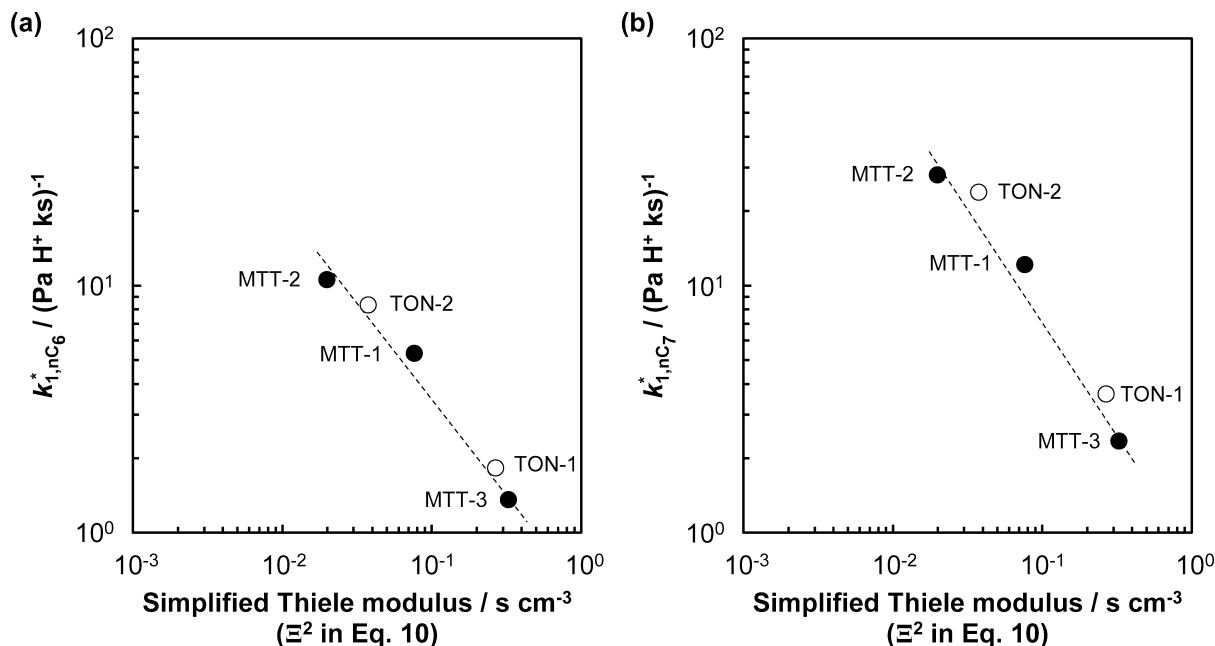


**Fig. 2.** Measured first-order rate constants (per  $H^+$ ; at 548 K) for (a)  $nC_6$  isomerization ( $k_{1,nC_6}^*$ ) and (b)  $nC_7$  isomerization ( $k_{1,nC_7}^*$ ) on MTT (filled; Table 1) and TON (open; Table 1) as a function of the squared simplified Thiele modulus ( $\Xi^2$ , Eq. (10)). Dashed lines represent trends.

Fig. 3 shows that these observed rate constant ratios ( $k_{1,nC_7}^*/k_{1,nC_6}^*$ ) on MTT and TON decrease (from 3.0 to 1.8) as  $\Xi^2$  increases (through changes in  $R^2/D_{np}$  and/or  $\rho_{H^+}$ ). These rate constant ratios on MTT and TON have nearly the same dependence on  $\Xi^2$ , as expected from their similar void environments (maximum diameter of a sphere that can diffuse along the crystallite, which we refer to as the pore-limiting diameter = 0.51 nm [23]); the similar geometry of MTT and TON frameworks also leads to similar confining interactions with each of the two transition states (for  $nC_7$  and  $nC_6$  isomerization), thus leading to ratios of intrinsic kinetic constants ( $k_{1,nC_7}/k_{1,nC_6}$ ) and to ratios of molecular diffusivi-

ties ( $D_{nC_7}/D_{nC_6}$ ) that are similar for these two frameworks. The trends evident in Fig. 3 reflect the higher reactivity and lower diffusivity for linear heptenes than linear hexenes, which results in stronger intracrystalline gradients of  $nC_7$  compared to  $nC_6$  in MTT and TON (Fig. 2a and b, respectively) and which reflect the involvement of protons throughout these diffusion-limited acid domains.

The presence and severity of these gradients can be assessed more rigorously using reaction-transport formalisms, by taking the ratio of  $k_{1,nC_7}^*$  to  $k_{1,nC_6}^*$  (using Eq. (9.2)). Such treatments show that the ratios of first-order rate constants for reactants that differ in size and reactivity are given by:

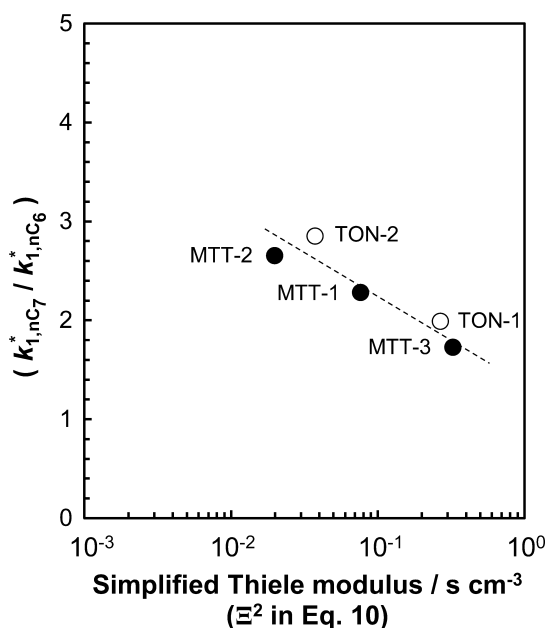


**Fig. 3.** Ratios of measured first-order rate constants ( $k_{1,nC_7}^*/k_{1,nC_6}^*$ ; at 548 K) on MTT (filled; Table 1) and TON (open; Table 1) as a function of the squared simplified Thiele modulus ( $\Xi^2$ , Eq. (10)). The dashed line represents trends.

$$\frac{k_{1,nC_7}^*}{k_{1,nC_6}^*} = \frac{\gamma_{nC_7} k_{1,nC_7}}{\gamma_{nC_6} k_{1,nC_6}} = \frac{k_{1,nC_7} \phi_{nC_6}^2 (\phi_{nC_7} \coth(\phi_{nC_7}) - 1)}{k_{1,nC_6} \phi_{nC_7}^2 (\phi_{nC_6} \coth(\phi_{nC_6}) - 1)}$$

$$= \frac{D_{nC_7}}{D_{nC_6}} \frac{\left( \Xi \sqrt{k_{1,nC_7} \frac{D_{np}}{D_{nC_7}}} \coth \left( \Xi \sqrt{k_{1,nC_7} \frac{D_{np}}{D_{nC_7}}} \right) - 1 \right)}{\left( \Xi \sqrt{k_{1,nC_6} \frac{D_{np}}{D_{nC_6}}} \coth \left( \Xi \sqrt{k_{1,nC_6} \frac{D_{np}}{D_{nC_6}}} \right) - 1 \right)} \quad (12)$$

for quasi-spherical acid domains. When neither reactant exhibits intracrystalline reactant gradients ( $\phi_{nC_7}^2, \phi_{nC_6}^2 \ll 1$ ), this ratio equals the ratio of their intrinsic kinetic constants ( $k_{1,nC_7}/k_{1,nC_6}$ ), which is larger than unity because the larger  $nC_7$  reactants form more stable carbocations at the isomerization transition state [21,32]. When both reactants exhibit severe intracrystalline gradients ( $\phi_{nC_7}^2, \phi_{nC_6}^2 \gg 1$ ), Eq. (12) becomes:

$$\frac{k_{1,nC_7}^*}{k_{1,nC_6}^*} = \sqrt{\frac{k_{1,nC_7} D_{nC_7}}{k_{1,nC_6} D_{nC_6}}} \quad (13)$$

This expression depends only on the intrinsic properties of the protons (acid strength) and of their “containers” (size, shape) but not on  $\Xi$  (Eq. (10)). Intracrystalline gradients would lead to smaller  $k_{1,nC_7}^*/k_{1,nC_6}^*$  ratios than the that of their intrinsic rate constants

( $k_{1,nC_7}/k_{1,nC_6}$ ) because linear heptenes diffuse more slowly than linear hexenes [30]. The form of Eq. (12) indicates that more severe gradients would lead to a monotonic decrease in  $k_{1,nC_7}^*/k_{1,nC_6}^*$  ratios from their intrinsic value ( $k_{1,nC_7}/k_{1,nC_6}$ ) to the values characteristic of severe intracrystalline gradients (Eq. (13)) as  $\Xi$  values increase. Indeed, measured rate constant ratios (Fig. 3) decrease as  $\Xi$  increases, consistent with the involvement of all intracrystalline protons instead of only those near pore mouths or at external surfaces, in which case all relevant protons would remain freely accessible to alkenes without regard for the chain length, reactivity, or diffusivity of the alkene reactants.

### 3.1.2. Intracrystalline concentration gradients of reactant alkenes during desorption of pre-adsorbed $NH_3$ titrants

In this section, the kinetic relevance of intrapore protons in 1-D 10-membered ring (MR) zeolites is demonstrated by comparing isomerization rates during the desorption of pre-adsorbed  $NH_3$  titrants for these materials and for other zeolites (14-MR, 1-D: SFH; 12-MR, 3-D: FAU, BEA; 10-MR, 3-D: MFI; Table 1), in which acid sites are located within larger channels and voids (12-MR and 14-MR structures) or within smaller voids in 10-MR structures but with three-dimensional connectivity that provides local cage-like voids larger than those within 1-D 10-MR channels. These less constrained voids allow more facile diffusion and typically give lower intrinsic reactivities because of the weaker confinement of transition states. This leads, in turn, to smaller  $\phi_{nC_7}$  and  $\phi_{nC_6}$  values (Eq. (8.1)) and to undetectable intracrystalline gradients of alkene reactants (as discussed later in this section and shown previously [5]).

The products formed from n-hexane/n-heptane reactant mixtures were measured as pre-adsorbed  $NH_3$  titrants gradually desorbed and the density of accessible protons ( $\rho_{H^+}$ ) and  $\Xi$  values (and thus  $\phi_{nC_7}$  and  $\phi_{nC_6}$  values) concurrently increased, thus causing any intracrystalline gradients of reactant (and product) alkenes to become more severe. Fig. 4a shows that the ratio of n-heptane to n-hexane isomerization rates ( $r_{isom,nC_7}/r_{isom,nC_6}$ ) on MFI remained constant (Fig. 4a; 3.2) as  $NH_3$  desorbed, even though  $nC_6$  and  $nC_7$

conversion rates both increased significantly as the titrant desorbed (by 10-fold; Fig. 4a;  $0.03\text{--}0.3\text{ mol. (kg ks)}^{-1}$  for  $nC_6$  and  $0.1\text{--}1.1\text{ mol. (kg ks)}^{-1}$  for  $nC_7$ ). On this MFI sample, neither linear heptenes nor the smaller and less reactive linear hexenes exhibit kinetically-consequential intracrystalline gradients, as shown by the similar  $nC_7$  isomerization rates measured on MFI samples with a wide range of  $\rho_{H^+}$  and  $R^2/D_{22DMB}$  values [5]. The absence of kinetically-consequential intracrystalline gradients of reactant alkene concentrations on MFI was confirmed here from  $r_{isom,nC_7}/r_{isom,nC_6}$  ratios that remained constant throughout the desorption of  $NH_3$  and the concomitant increase in the density of untrapped protons.

Isomerization rates and  $r_{isom,nC_7}/r_{isom,nC_6}$  ratios on FAU, SFH, and BEA showed similar trends with the extent of  $NH_3$  desorption as the MFI sample (Supporting Information Section S1). The  $r_{isom,nC_7}/r_{isom,nC_6}$  ratios remained constant (3.3–3.5) as  $r_{isom,nC_7}$  and  $r_{isom,nC_6}$  both increased as the number of accessible protons increased (FAU:  $0.09\text{--}0.4$  and  $0.03\text{--}0.1\text{ mol (kg ks)}^{-1}$  for  $nC_7$  and  $nC_6$ ; SFH:  $0.05\text{--}0.25$  and  $0.01\text{--}0.07\text{ mol (kg ks)}^{-1}$ ; and BEA:  $0.6\text{--}1.6$  and  $0.2\text{--}0.6\text{ mol (kg ks)}^{-1}$ ; Supporting Information Section S1). These data confirm that  $nC_7$  and  $nC_6$  isomerization rates on FAU, SFH, and BEA are also unaffected by intracrystalline gradients of reactant alkenes, which would have led to rate ratios that would vary as titrants desorbed. These  $r_{isom,nC_7}/r_{isom,nC_6}$  ratios reflect the intrinsic reactivity difference between linear heptene and hexene regioisomers within each given void structure. The  $r_{isom,nC_7}/r_{isom,nC_6}$  ratios are similar among these materials (3.2–3.5), even though voids differ nearly two-fold in size (diameter of the largest contained sphere,  $d_{LC} = 1.1\text{ nm}$  for FAU,  $0.76\text{ nm}$  for SFH,  $0.67\text{ nm}$  for BEA, and  $0.64\text{ nm}$  for MFI [23]). These  $r_{isom,nC_7}/r_{isom,nC_6}$  ratios are shown as a function of the  $d_{LC}$  for FAU, SFH, BEA, and MFI in the Supporting Information (Section S1). The effects of solvation by confinement on the stability of  $nC_7$  isomerization transition states led to ten-fold differences in their intrinsic  $k_{1,nC_7}$  values (e.g.  $8.9$  vs.  $99\text{ (Pa H}^+\text{ ks)}^{-1}$  for FAU and MFI, respectively [5]). These different  $k_{1,nC_7}$  values arise from the more effective van der Waals contacts between the inorganic

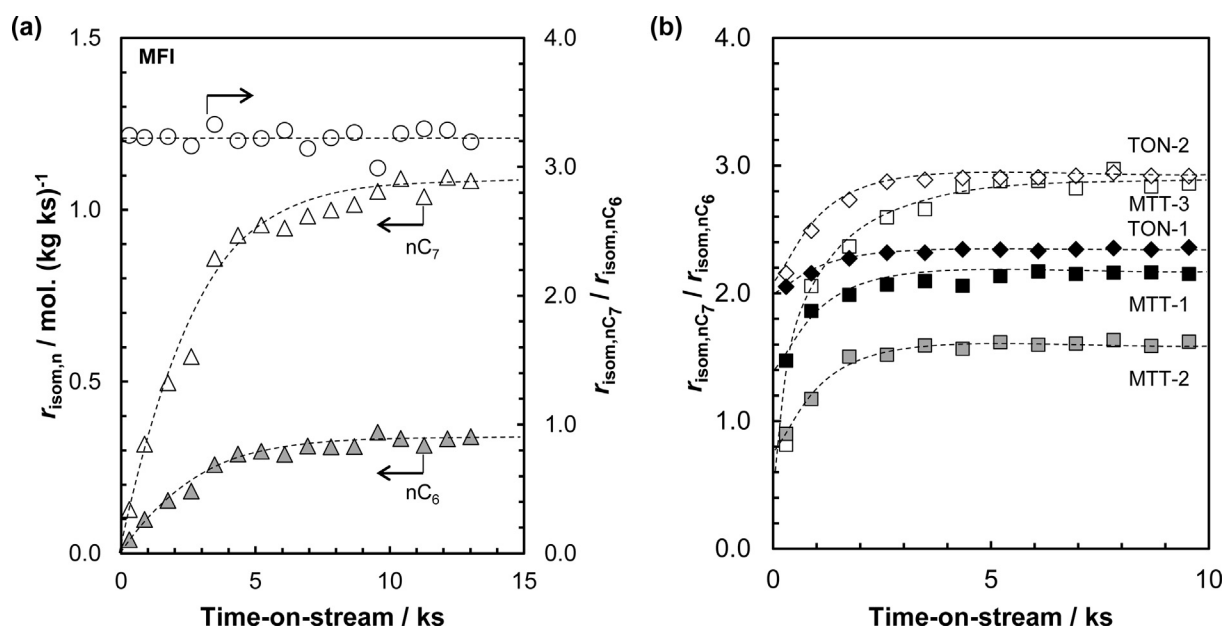


**Fig. 4.** (a) n-Heptane isomerization rates ( $r_{isom,nC_7}$ , left ordinate; white triangles), n-hexane isomerization rates ( $r_{isom,nC_6}$ , left ordinate; grey triangles), and rate ratios ( $r_{isom,nC_7}/r_{isom,nC_6}$ , right ordinate; circles) as a function of time-on-stream during  $NH_3$  desorption on MFI and (b) rate ratios ( $r_{isom,nC_7}/r_{isom,nC_6}$ ) as a function of time-on-stream during  $NH_3$  desorption on TON (diamonds) and MTT (squares) samples (200  $H_2/nC_6$  molar ratio, 200  $H_2/nC_7$  molar ratio, 100 kPa  $H_2$ , 548 K). Dashed lines represent trends.

framework and the transition state carbocation in MFI compared with FAU voids; the effectiveness of such van der Waals contacts varies with void size, but seems to do so with similar consequences for the nC<sub>7</sub> and nC<sub>6</sub> isomerization transition states.

The dimensions of the relevant transition state carbocations for nC<sub>6</sub> and nC<sub>7</sub> isomerization can be estimated from their DFT-derived structures. These transition state structures were optimized at the T12 crystallographic site in MFI [5], but the sizes and trends are similar at other locations. The transition state diameter is defined as that of the sphere of equivalent volume ( $d_{\text{eq}} = 6V/A_s$ , where  $V$  is volume and  $A_s$  is surface area) or equivalent surface area ( $d_{\text{eq,SA}} = \sqrt{A_s/\pi}$ ). These diameters are slightly smaller for nC<sub>6</sub> ( $d_{\text{eq}} = 0.60$  or  $d_{\text{eq,SA}} = 0.65$  nm) than nC<sub>7</sub> ( $d_{\text{eq}} = 0.64$  or  $d_{\text{eq,SA}} = 0.70$  nm) transition states [5], suggesting that these two structures would sense the confining voids through dispersion interactions to a slightly different extent. These alkyl-substituted cyclopropyl carbocations are ellipsoidal in shape and differ for reactions of nC<sub>6</sub> and nC<sub>7</sub> only in their respective axial dimensions, which, taken together with the complex topology of the void space, render metrics of size based on spherical constructs imprecise in accounting for the effectiveness of van der Waals contacts [5,33]. Even more rigorous descriptors based on host-guest interaction energies [5,33] must also account for energy penalties incurred as frameworks distort to minimize transition state free energies [5,34]. The weak effects of two-fold changes in void size on  $r_{\text{isom,nC}_7}/r_{\text{isom,nC}_6}$  ratios indicate that similar  $r_{\text{isom,nC}_7}/r_{\text{isom,nC}_6}$  values are thus expected for MTT and TON in the absence of intracrystalline gradients, because of their similar confining structures ( $\sim 0.51$  nm [23]).

Fig. 4b shows  $r_{\text{isom,nC}_7}/r_{\text{isom,nC}_6}$  ratios on MTT and TON as NH<sub>3</sub> titrants desorb during reactions. These ratios are 0.8–2.0 when extrapolated to the initial stages of NH<sub>3</sub> desorption for these samples and quickly reached constant values similar to those measured before exposure to the NH<sub>3</sub> titrants (1.4–3.0); as expected, these rate ratios are the same as the measured first-order rate constant ratios ( $k_{1,\text{nC}_7}^*/k_{1,\text{nC}_6}^* = 1.7\text{--}2.9$ , Fig. 3), after accounting for differences in the gas-phase nC<sub>6</sub> and nC<sub>7</sub> dehydrogenation equilibrium constants ( $K_{\text{dehyd,nC}_7}/K_{\text{dehyd,nC}_6} = 1.1$ ). These rate ratios increase during NH<sub>3</sub> desorption because intracrystalline gradients develop first for n-heptenes and ultimately for n-hexenes as proton densities increase upon gradual NH<sub>3</sub> desorption, because of the lower reactivity and higher diffusivity of n-hexenes ( $k_{1,\text{nC}_6} < k_{1,\text{nC}_7}$ ;  $D_{\text{nC}_6} > D_{\text{nC}_7}$ ). This leads to weaker intracrystalline gradients for n-hexenes than n-heptenes ( $\phi_{\text{nC}_6} < \phi_{\text{nC}_7}$ , Eq. (8.1)) at each given  $\rho_{\text{H}^+}$  value (as NH<sub>3</sub> desorbs) and to n-hexene isomerization rates (per H<sup>+</sup>) that are less sensitive than n-heptene isomerization rates to changes in intracrystalline proton density ( $\rho_{\text{H}^+}$ ) as NH<sub>3</sub> desorbs.

The  $r_{\text{isom,nC}_7}/r_{\text{isom,nC}_6}$  ratios for a given sample are expected to be least affected by intracrystalline alkene gradients when extrapolated to initial times (0.6–2.0, Fig. 4b), because  $\rho_{\text{H}^+}$ ,  $\phi_{\text{nC}_7}$ , and  $\phi_{\text{nC}_6}$  are smallest in this asymptotic limit. These asymptotic rate ratios vary among MTT and TON samples with different  $\Xi^2$  values (0.02–0.33; Eq. (10)) by two-fold and three-fold, respectively ( $r_{\text{isom,nC}_7}/r_{\text{isom,nC}_6} = 0.6\text{--}1.2$  for MTT; 0.8–2.0 for TON), indicative of effects of intracrystalline gradients, because intrinsic rate constant ratios would not be expected to depend on  $\rho_{\text{H}^+}$  or  $R^2/D_{\text{np}}$  and should resemble those on FAU, SFH, BEA, and MFI (3.2–3.5). These differences indicate that n-heptene intracrystalline gradients influence measured rates on MTT and TON even at these very small  $\rho_{\text{H}^+}$  values (and thus,  $\phi_{\text{nC}_7}$  values) because of the very severe diffusional hurdles imposed by the one-dimensional nature of these 10-MR frameworks [12–14].

The  $r_{\text{isom,nC}_7}/r_{\text{isom,nC}_6}$  ratios on all TON and MTT samples increase during the early stages of NH<sub>3</sub> desorption from these asymptotic values, as a result of nC<sub>6</sub> isomerization rates reflect that nC<sub>6</sub> rates

are less affected by intracrystalline concentration gradients than nC<sub>7</sub> rates at such low proton densities. Rate ratios on all TON and MTT samples ultimately become independent of intracrystalline proton densities. These increases in rate ratios for TON and MTT as NH<sub>3</sub> desorbs provide additional support for the conclusion that intrapore protons all contribute to catalytic turnovers.

In the next section, the products formed in reactions of nC<sub>6</sub> and nC<sub>7</sub> during NH<sub>3</sub> desorption are examined in order to assess how intracrystalline gradients of isoalkene products (in addition to those of n-alkene reactants) lead to secondary interconversions and to the preferential formation of isomer products with a single methyl group near the end of their backbones. Such unusual selectivities are shown to merely reflect the faster diffusion of 2-methyl isomers than other products and the absence of framework undulations that can locally retain more highly branched isomers and enhance their secondary  $\beta$ -scission reactions; such phenomena account for selectivities previously attributed to the partial entry of n-alkenes into channels and their preferential reactions at protons near the “pore-mouth” of one-dimensional 10-MR zeolite crystallites [8–11].

### 3.2. Intracrystalline concentration gradients of isoalkene products, their diffusion-enhanced interconversions, and their consequences for measured selectivities

The higher reactivity and slower diffusion of isoalkenes relative to their n-alkene precursors cause strong effects of intracrystalline gradients on selectivity as a result of diffusion-enhanced secondary isoalkene interconversions within acid domains [5–7]. The isoalkene concentration gradients and their strong kinetic consequences are most evident for protons within one-dimensional 10-MR microporous aluminosilicates, but influence selectivities even on zeolite crystallites that lack kinetically-consequential gradients of the n-alkene reactants (FAU, SFH, BEA, and MFI; Section 3.1.2). The consequences of diffusion-enhanced secondary reactions on isomer products and  $\beta$ -scission selectivities are assessed here using experiments that vary the bed residence time for a mesoporous solid acid without significant diffusional hurdles (Al-MCM-41) and for two one-dimensional 10-MR zeolites that impose significant intracrystalline gradients even for the n-alkene reactants (TON and MTT with a range of  $R^2/D_{\text{np}}$  and  $\rho_{\text{H}^+}$ ).

Fig. 5a shows measured 2MH/3MH isomer ratios ( $S_{2\text{MH}/3\text{MH}}$ ) using nC<sub>7</sub> reactants on these catalysts as a function of changes in reactant conversion resulting from changes in bed residence time. The  $S_{2\text{MH}/3\text{MH}}$  values at low conversions are higher on Al-MCM-41 than expected from the equilibration of either these two methylhexanes ( $S_{2\text{MH}/3\text{MH,eq}} = 0.88$  at 548 K [20,24]) or their respective methylhexene regioisomers ( $S_{2\text{MH}/3\text{MH,eq}} = 0.47$  at 548 K [20,24]; calculations of equilibrium ratios in the Supporting Information Section S2). These asymptotic isomer ratios reflect the formation of both 2MH<sup>+</sup> and 3MH<sup>+</sup> skeletal isomers in primary events, but with a greater preference for 2MH<sup>+</sup> than 2MH<sup>+</sup>–3MH<sup>+</sup> (or 2MH–3MH) equilibration would dictate. These data are consistent with the smaller DFT-derived transition state free energies for nC<sub>7</sub> conversion to 2MH<sup>+</sup> than to 3MH<sup>+</sup> (by about 6 kJ mol<sup>−1</sup> [5]), which causes the preferential formation of 2MH<sup>+</sup> over 3MH<sup>+</sup> in each single-sojourn isomerization event.

These  $S_{2\text{MH}/3\text{MH}}$  values decrease with increasing bed residence times on Al-MCM-41 and approach the equilibrium value for the interconversion of the two methylhexanes (Fig. 5a). These trends reflect the diffusion of the primary 2MH<sup>+</sup> and 3MH<sup>+</sup> isomers through Al-MCM-41 mesopores and into the fluid phase before complete 2MH<sup>+</sup>–3MH<sup>+</sup> equilibration within the acid domain in which they initially formed. These isomers reach hydrogenation-dehydrogenation equilibrium at the metal function, and 2MH<sup>+</sup>

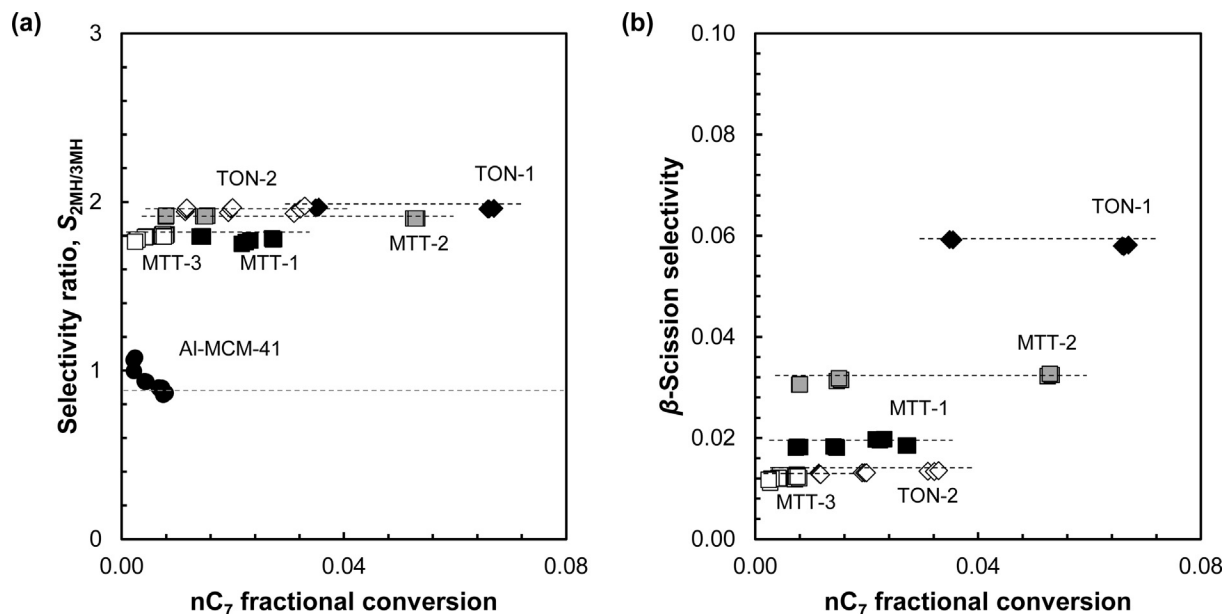


**Fig. 5.** (a) Ratio of selectivities for 2-methylhexane and 3-methylhexane ( $S_{2MH/3MH}$ ) for Al-MCM-41, MTT-1–3, and TON-1–2 and (b)  $\beta$ -scission selectivities during n-heptane reactions on physical mixtures of Al-MCM-41 (circles), MTT-1–3 (squares), and TON-1–2 (diamonds) with Pt/SiO<sub>2</sub> as a function of fractional n-heptane conversion, varied through changes in reactant space velocity (35–165 molec. (H<sup>+</sup> ks)<sup>-1</sup> space velocity, 0.01 nC<sub>7</sub>/H<sub>2</sub> molar ratio, 548 K). The black dashed lines represent trends; the dot-dash line in (a) represents the selectivity ratio expected for equilibrated mixtures of 2MH and 3MH as alkanes.  $\beta$ -Scission products were below detection limits on Al-MCM-41 at all residence times.

and 3MH<sup>-</sup> freely re-enter acid domains along the bed and interconvert, ultimately leading to equilibrated mixtures of methylhexanes (methylhexenes are not detectable at their equilibrium concentrations with the respective alkane) through sequential sojourns in Al-MCM-41 acid domains as they traverse the bed. These bed residence time effects cause  $S_{2MH/3MH}$  values to approach those predicted from alkane thermodynamics ( $S_{2MH/3MH,eq}$ ). The facile (and bidirectional) nature of diffusion within Al-MCM-41 allows egress before equilibration, but also the opportunity for subsequent sojourns at intracrystalline acid sites along the bed.

In marked contrast with the behavior of mesoporous Al-MCM-41 acids,  $S_{2MH/3MH}$  ratios on MTT and TON are insensitive to bed residence time (Fig. 5a) and exceed equilibrium ratios for methylhexenes ( $S_{2MH/3MH,eq}$ ) or methylhexanes ( $S_{2MH/3MH,eq}$ ). These  $S_{2MH/3MH}$  values are very similar on TON (1.9–2.0) and MTT (1.7–1.9), apparently because of the similar size, shape, and connectivity of their 1-D channels, which impose similar diffusional hurdles and confinement effects (Section 3.1). These constant  $S_{2MH/3MH}$  ratios indicate that isoalkene products that egress from a given TON or MTT crystallite do not interconvert by re-entry and reaction at crystallites along the bed. The strong prevalent intracrystalline gradients lead to intracrystalline isoalkene concentrations that are much higher within acid domains than in the extracrystalline fluid phase. This leads to essentially unidirectional diffusive flow, thus precluding downstream domains from detecting the molecules in the fluid phase formed within preceding domains. These strong intracrystalline gradients reflect the higher reactivity and lower diffusivity of highly branched product isoalkenes [7] relative to the linear alkenes from which they formed. The egress of isoalkenes from each acid domain can be considered essentially irreversible as strong diffusional hurdles are imposed by small one-dimensional channels; in contrast, the much larger mesopores in Al-MCM-41 aluminosilicates allow unhindered bidirectional transport between the fluid and the intracrystalline regions and the full equilibration of methyl isomers and of isoalkenes and isoalkanes.

$\beta$ -Scission occurs only via secondary reactions of 2,4-dimethylpentene isomers [5,7] that diffuse even more slowly than

methylhexenes, leading to  $\beta$ -scission selectivities on TON and MTT that also “detect” the presence of intracrystalline gradients, as shown by the effects of  $\Xi$  (Eq. (10); Table 1) on these  $\beta$ -scission selectivities (Fig. 5b).  $\beta$ -Scission products are detectable at all  $nC_7$  conversions; their selectivities are insensitive to bed residence time on TON and MTT but increase with increasing  $\Xi$  values (Eq. (10);  $\beta$ -scission selectivities increased from 0.012 to 0.060, as  $\Xi^2$  decreased from 0.33 to 0.02; Fig. 5b) and as NH<sub>3</sub> titrants desorb and intracrystalline gradients of dimethylpentene products become more severe (discussed in Section 3.2.1). In contrast,  $\beta$ -scission products were not detected on Al-MCM-41, even at the highest  $nC_7$  conversions, because intracrystalline dimethylpentene concentrations are in equilibrium with those in the fluid phase and much lower than those in the intracrystalline spaces of MTT and TON crystallites. These  $\beta$ -scission selectivities and the specificity of the methyl position in isoalkanes on these 1-D 10-MR channel systems differ from those on large-pore zeolite frameworks (FAU, SFH, BEA), a reflection of the uniquely restricted environments provided by aluminosilicates with one-dimensional 10-MR channels.

Selectivity ratios are examined next on FAU, SFH, and BEA as NH<sub>3</sub> titrants desorb and the density of protons and the severity of product gradients concomitantly increase (Eq. (8.1) and (8.2)). Fig. 6a shows  $S_{2MH/3MH}$  and  $S_{2MP/3MP}$  and  $\beta$ -scission selectivities from n-heptane/n-hexane mixtures on FAU as NH<sub>3</sub> desorbs (Supporting Information Section S3 shows  $S_{2MH/3MH}$  and  $S_{2MP/3MP}$  and  $\beta$ -scission selectivities on BEA and SFH); the abscissa is defined as the  $nC_6$  conversion rate at any point in time as a fraction of the rate measured before contact with NH<sub>3</sub> (or after its complete desorption) ( $\chi(t)$ , Eq. (4)). These  $\chi(t)$  values act as an accurate surrogate for the fraction of the protons that become uncovered (and thus available for reaction) as NH<sub>3</sub> desorbs when isomerization rates are unaffected by intracrystalline gradients of reactant-derived alkenes, as is the case for FAU, SFH, BEA, and MFI (discussed in Section 3.1.2). When intracrystalline gradients are present (i.e., for MTT and TON in this study), rates become instead proportional to  $(\rho_{H^+})^{0.5}$  in the asymptotic limit of severe gradients, leading to  $\chi(t)$  values that remain a directional (but no

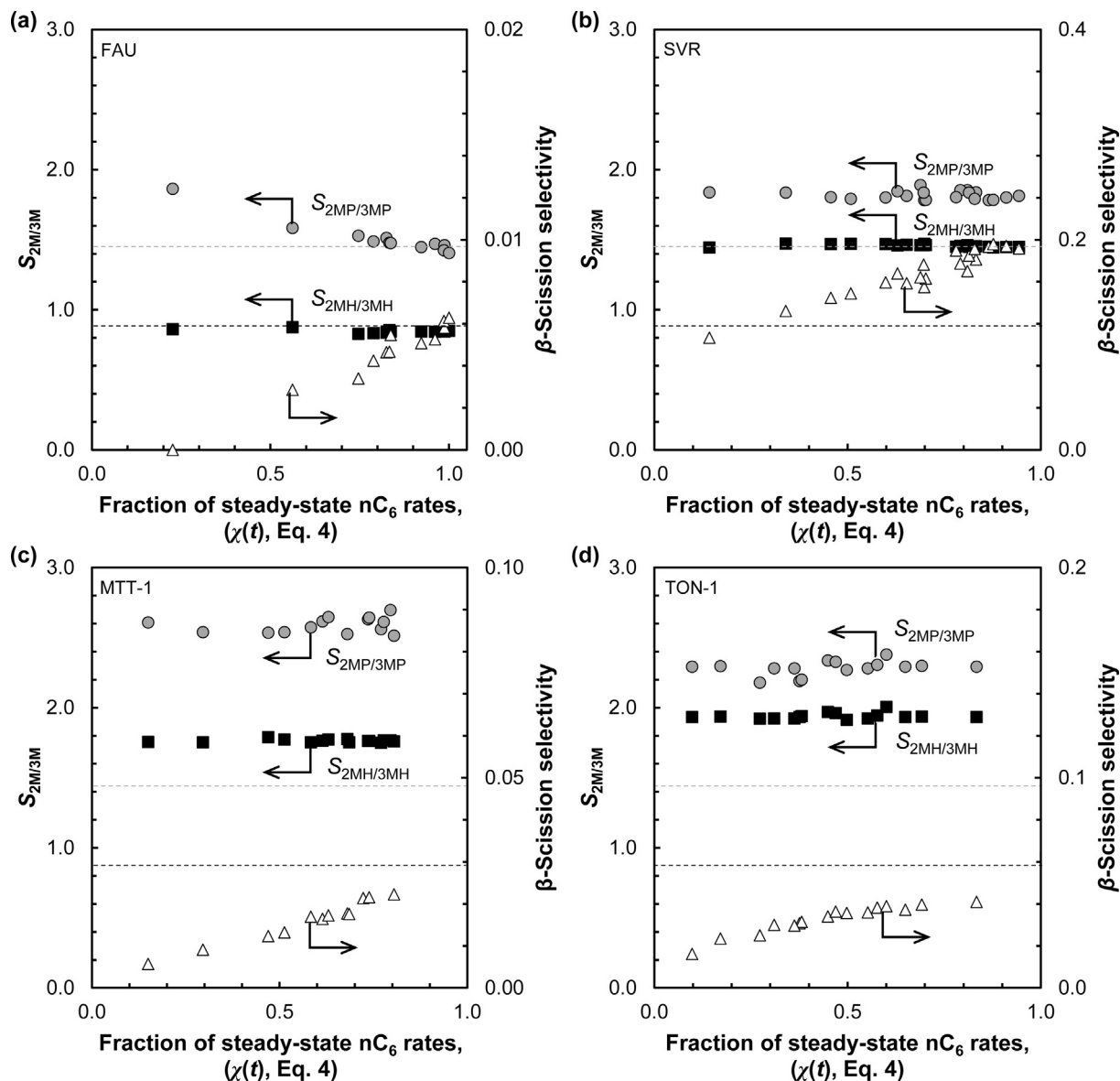


**Fig. 6.** Selectivity ratio for 2-methylhexane to 3-methylhexane ( $S_{2MH/3MH}$ , circles, left ordinate) and for 2-methylpentane to 3-methylpentane ( $S_{2MP/3MP}$ , squares, left ordinate) and selectivity to  $\beta$ -scission products (triangles, right ordinate) on (a) FAU, (b) SVR, (c) MTT-1, and (d) TON-1 as a function of fraction of steady-state  $nC_6$  rate ( $\chi(t)$ , Eq. (4)) during  $NH_3$  desorption (200  $H_2/nC_6$  molar ratio, 200  $H_2/nC_7$  molar ratio, 100 kPa  $H_2$ , 548 K). Dashed lines represent selectivity ratios expected for equilibrated mixtures of 2MH and 3MH (black) and 2MP and 3MP (grey).

longer proportional) indicator of the fraction of protons that become accessible as  $NH_3$  desorbs.

On large-pore zeolites, such as FAU, SFH, and BEA,  $\beta$ -scission products were not detected from  $nC_7$  reactants at low  $\chi(t)$  values (Fig. 6a for FAU; Supporting Information Section S3 for SFH and BEA); they increased, however, as  $NH_3$  desorbed and  $\chi(t)$  increased, consistent with diffusion-enhanced  $\beta$ -scission reactions of dimethylpentenes as  $\rho_{H^+}$  and  $\phi_n$  increase and intracrystalline dimethylpentene concentrations become increasingly higher than in the fluid phase. Yet,  $S_{2MH/3MH}$  ratios do not change with  $\chi(t)$  (Fig. 6a) on FAU (and on SFH and BEA; Supporting Information Section S3) and correspond to those for equilibrium mixtures of 2-methyl and 3-methyl hexanes ( $S_{2MH/3MH,eq}$ ); these data are indicative of weak intracrystalline gradients of 2-methyl and 3-methyl hexenes isomers within these large-pore zeolite crystallites. This merely reflects the smaller diffusivities for dimethylpentenes than methylhexenes, which lead to gradients that are kinetically-consequential for the dimethylpentene isomers involved in  $\beta$ -

scission, but not for the interconversion of the faster-diffusing methylhexenes.

Similar trends and mechanistic interpretations are evident for the observed effects of  $NH_3$  desorption on the methyl pentanes formed as primary isomer products of  $nC_6$  reactions (as mixtures with  $n$ -heptane). The initial  $S_{2MP/3MP}$  ratios (as  $\chi(t) \rightarrow 0$ ) on FAU (2, Fig. 6a) are larger than equilibrium ratios ( $S_{2MP/3MP,eq} = 1.38$  and  $S_{2MP=3MP,eq} = 1.44$  at 548 K, calculated using tabulated thermodynamic data [20,24]) but approach these equilibrium ratios as  $NH_3$  desorbs and  $\chi(t)$  increases; for BEA and SFH (Supporting Information Section S3),  $S_{2MP/3MP}$  ratios are independent of  $NH_3$  desorption and have values equal to selectivities expected for alkane (2MP–3MP) equilibration. These trends for FAU reflect the preferential formation of  $2MP^{\ddagger}$  over  $3MP^{\ddagger}$  in single-sojourn events by  $nC_6^{\ddagger}$  reactants [35], as a consequence of the relative stability of the cyclopropyl carbocations at their respective transition states. These  $nC_6$  alkenes are less reactive (as shown in Section 3.1) and diffuse faster [36,37] than  $nC_7$  alkenes, leading to their weaker

intracrystalline gradients (than  $nC_7$  alkenes) and to  $S_{2MP/3MP}$  values that reflect the extracrystalline equilibration of alkenes with their respective alkanes.

As the confining voids become smaller, from large-pore zeolites (FAU, SFH, BEA) to 10-MR zeolites (MEL, MFI, SVR, MTT, and TON), selectivity ratios no longer reflect the equilibration of the hydrogenated analogs of methylhexene or methylpentene intermediates; these are the same phenomena underlying the selectivity ratios for MTT and TON that were discussed previously in this section. The effects of  $NH_3$  desorption on  $S_{2MH/3MH}$  and  $S_{2MP/3MP}$  ratios for 10-MR zeolites are examined next using detailed reaction-transport treatments in order to demonstrate how the unique sieving ability of zeolites causes intracrystalline concentration gradients that vary sensitively with backbone structure, thus rendering the “emission” of certain species from acid domains essentially irreversible and strongly favoring the egress of 2-methyl isomers into the convective fluid phase.

### 3.2.1. Isomer sieving in diffusion-enhanced secondary interconversions and consequences for the location of the methyl groups in isoalkanes

Fig. 6 shows  $S_{2MH/3MH}$  and  $S_{2MP/3MP}$  ratios and  $\beta$ -scission selectivities on SVR (Fig. 6b), MTT (Fig. 6c; MTT-1 as the illustrative MTT sample), and TON (Fig. 6d; TON-1 as the illustrative TON sample) for  $nC_6$  and  $nC_7$  mixtures during  $NH_3$  desorption. The corresponding data on MEL and MFI are included in the Supporting Information (Section S3).

The  $S_{2MH/3MH}$  values for each given zeolite (MEL: 1.3, MFI: 1.4, SVR: 1.5, MTT: 1.9, TON: 2.0) did not change as  $NH_3$  desorbed and  $\chi(t)$  increased, but they differed from the  $S_{2MH/3MH,eq}$  values expected from equilibration among methylhexanes (0.88). The  $S_{2MH/3MH}$  values were nearly identical on all MTT and TON samples (1.87–1.92 for MTT, 1.93–2.02 for TON); they reflect the rate at which equilibrated methylhexenes are “sieved” by a given void structure and egress into the extracrystalline fluid media, where they hydrogenate at the Pt function and are then detected in the effluent stream. 2-Methyl alkenes are sieved preferentially over 3-methyl alkenes because they diffuse faster, as indicated by reported diffusivities and the reaction-transport models described next.

These isomer sieving effects can be assessed based on Thiele moduli ( $\phi_{2MH}^2$  and  $\phi_{3MH}^2$ ) that describe the formation and interconversion of  $2MH^-$  and  $3MH^-$  regioisomers during  $nC_7$  isomerization using the same formalisms that describe the consequences of  $n$ -alkene reactant concentration gradients on isomerization rates (Section 3.1.1):

$$\phi_{2MH}^2 = \frac{k_{2MH} \rho_{H^+} R^2}{D_{2MH}} \quad (13.1)$$

$$\phi_{3MH}^2 = \frac{k_{3MH} \rho_{H^+} R^2}{D_{3MH}} \quad (13.2)$$

Here,  $k_{2MH}$  and  $k_{3MH}$  represent the first-order rate constants for the forward and reverse conversion of  $2MH^-$  to  $3MH^-$ , respectively;  $D_{2MH}$  and  $D_{3MH}$  are the mean diffusivities for the equilibrated pool of regioisomers of  $2MH^-$  and  $3MH^-$ , respectively. These Thiele parameters and the intracrystalline mole balances used to obtain them describe the rate of egress of each isoalkene from an acid domain of a given size ( $R$ ) and volumetric proton density ( $\rho_{H^+}$ ); these isoalkenes are ultimately detected as their respective isoalkanes upon hydrogenation at the extracrystalline metal function. These mole balances and Thiele moduli are used here for molecules and conditions, such as those in this study, that lead to the formation of dimethylalkenes and  $\beta$ -scission products at much lower rates than for  $2MH^-$ - $3MH^-$  interconversions.

The  $S_{2MH/3MH}$  ratios derived from these treatments (derivations in Supporting Information Section S4) show two asymptotic limits that are defined by the magnitude of  $\phi_{2MH}^2$  and  $\phi_{3MH}^2$ . When  $2MH^-$  and  $3MH^-$  do not exhibit intracrystalline concentration gradients ( $\phi_{2MH}^2, \phi_{3MH}^2 \ll 1$ ), these ratios merely reflect the ratio of intrinsic rate constants for their respective formation from  $nC_7^-$  regioisomers:

$$S_{2MH/3MH} = \frac{k_{1,nC_7 \rightarrow 2MH^-}}{k_{1,nC_7 \rightarrow 3MH^-}} \quad (14)$$

where  $k_{1,nC_7 \rightarrow 2MH^-}$  and  $k_{1,nC_7 \rightarrow 3MH^-}$  are the first-order rate constants for  $nC_7^-$  isomerization to  $2MH^-$  and  $3MH^-$ , respectively. These ratios represent the intrinsic (single-sojourn) selectivity to the two methyl isomers from  $n$ -heptenes, but facile secondary methyl shifts before hydrogenation preclude their detection for all zeolites. Only at very short residence times on Al-MCM-41 (Fig. 5a), a mesoporous aluminosilicate that exhibits low reactivity because of weak van der Waals interactions at isomerization transition states, are selectivity ratios larger than equilibrium values, indicative of the detection of single-sojourn events that favor  $2MH^-$  as the initial product of  $nC_7^-$  isomerization (as shown by theoretical assessments of the relevant transition states; [5]). As residence times increase on Al-MCM-41, secondary reactions (Section 3.2) cause selectivity ratios to approach those predicted by thermodynamics.

In the asymptotic limit leading to strong intracrystalline gradients of 2-methyl and 3-methyl alkenes ( $\phi_{2MH}^2, \phi_{3MH}^2 \gg 1$ ),  $S_{2MH/3MH}$  ratios (derived in Supporting Information Section S4) are:

$$S_{2MH/3MH} = [K_{2MH=3MH}] \left[ \frac{D_{2MH}}{D_{3MH}} \right] \quad (15)$$

where  $K_{2MH=3MH}$  is the  $2MH^-$ - $3MH^-$  interconversion equilibrium constant and equals  $S_{2MH=3MH,eq}$ .  $S_{2MH/3MH}$  values are given by the ratio of the respective diffusivities and of the equilibrium concentration ratio. These asymptotic limits can be derived similarly for  $2MP^-$ - $3MP^-$  interconversions ( $\phi_{2MP}^2$  and  $\phi_{3MP}^2$ , by analogy to Eqs. (13.1) and (13.2)); they are included explicitly in the Supporting Information (Section S4).

$S_{2MH/3MH}$  values that remain constant with bed residence time (Fig. 5a for TON and MTT) reflect the essentially irreversible emission of isoalkenes from acid domains caused by strong intracrystalline gradients ( $\phi_{2MH}^2, \phi_{3MH}^2 \gg 1$ ; Eqs. (13.1) and (13.2)), which lead to  $S_{2MH/3MH}$  values larger than expected for alkane equilibration; they reflect instead the thermodynamics of isoalkene interconversion and the ratio of diffusivities for  $2MH^-$  and  $3MH^-$  regioisomers (Eq. (15)).

These diffusivity ratios can be directly extracted from approach to equilibrium values ( $\eta$ ; Eq. (1)) and  $S_{2MH/3MH}$  values (Eq. (15)):

$$\eta_{2MH=3MH} = \left[ \frac{D_{2MH}}{D_{3MH}} \right] \quad (16)$$

(and analogously for  $2MP^-$ - $3MP^-$ ). Fig. 7 shows  $\eta$  values for  $2MH^-$ - $3MH^-$  ( $\eta_{2MH=3MH}$ , Eq. (1)) and  $2MP^-$ - $3MP^-$  ( $\eta_{2MP=3MP}$ , Eq. (1)) interconversions on 10-MR zeolites with different aperture diameters (pore-limiting diameter,  $d_{pl}$  [23]), calculated from the measured pressures of the alkane products, which reflect the pressures of the corresponding alkenes. The  $\eta_{2MH=3MH}$  values are similar among different MTT and TON samples (3.9–4.1 for MTT and 4.0–4.2 for TON) with different  $\rho_{H^+}$  and  $R^2/D_{np}$  values (Table 1). These constant values are shown in Fig. 7 as the mean value for each framework. The mean  $\eta_{2MP=3MP}$  values for  $nC_6$  reactants are also reported for these MTT and TON acids in Fig. 7 (1.8–1.9 for MTT and 1.6–1.7 for TON).

As voids become smaller in three-dimensional 10-MR frameworks (in the order MEL, MFI, SVR),  $\eta_{2MP=3MP}$  values

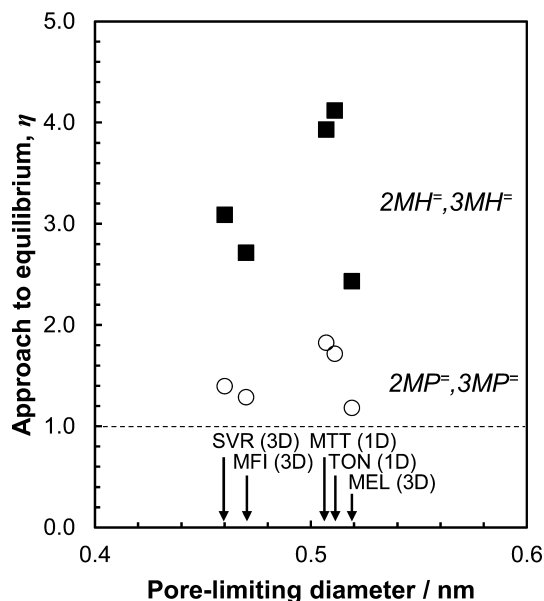


**Fig. 7.** Approach to equilibrium values for  $2MH^-$ - $3MH^-$  ( $\eta_{2MH^-,3MH^-}$ ; squares) and for  $2MP^-$ - $3MP^-$  ( $\eta_{2MP^-,3MP^-}$ ; circles) on each 10-MR zeolites as a function of zeolite pore-limiting diameter [23]. Values for MTT and TON are the mean value for all samples of each framework.

monotonically increase, consistent with a stronger preference for 2-methyl isomers as diffusional effects become more severe. Such trends are evidence whether diffusional constraints are exacerbated by the use of larger molecules (isoheptenes vs. isohexenes) or by smaller apertures within these three-dimensional zeolites (MEL, MFI, SVR) (Fig. 7). For all 10-MR zeolites,  $\eta$  values and selectivity ratios (Fig. 6b–d and Supporting Information Section S3) remained constant as  $\chi(t)$  increases and  $NH_3$  desorbs. These trends are more pronounced for  $\eta_{2MH^-,3MH^-}$  than for  $\eta_{2MP^-,3MP^-}$  because of the larger size of the methylhexenes compared to the methylpentenes.

Isoalkene diffusivity ratios depend on the size [30] and connectivity [38] of the void structure and on alkene size [36,37], most sensitively as molecules and apertures become similar in size [30,36,37]. For instance, 2,2-dimethylbutane diffusivities are  $\sim 10^3$  times smaller than that for benzene (0.585 nm kinetic diameter [36]) on MFI ( $2 \times 10^{-12}$  vs.  $7 \times 10^{-9}$  cm<sup>2</sup>/s at 423 K [36]), because the kinetic diameter of 2,2-dimethylbutane (0.62 nm) approaches the sizes of the 10-MR channels in MFI. Diffusivity ratios can be examined further for MFI. Alkene diffusivities are seldom measurable for acid forms of zeotypes because of their high oligomerization reactivity. As a result, diffusivities for their alkane analogs are used here to examine diffusivity trends, for MFI structures. The 2MP/3MP diffusivity ratio is 1.3 ( $D_{2MP}/D_{3MP}$  on MFI (Silicalite-1), extrapolated to 548 K using data at 376–476 K [37]). This value is similar to the  $\eta_{2MP^-,3MP^-}$  for MFI in Fig. 7 (1.3), which reflects the ratio of  $D_{2MP^^-}$  to  $D_{3MP^^-}$  (Eq. (16)); such agreement between these values confirms the accuracy of the reaction-transport model derived here.

Literature diffusivities for a given molecule differ among zeolite samples of the same framework [38], in part because of inaccurate visual assessments of crystallite size from micrographs. Nevertheless, the trends observed in  $\eta_{2MP^-,3MP^-}$  and  $\eta_{2MH^-,3MH^-}$  values (Fig. 7) are consistent with expectations of changes in diffusivities and diffusivity ratios; channel apertures in SVR are slightly smaller than in MFI (0.46 vs. 0.47 nm [23]) and become closer to the diameters of 2MP<sup>-</sup> and 3MP<sup>-</sup> molecules and  $\eta_{2MP^-,3MP^-}$  values are indeed slightly smaller for MFI than SVR (1.3 vs. 1.4); these ratios are even smaller for MEL (1.15), a framework with larger apertures (0.52 nm [23]). One-dimensional MTT and TON zeolites give  $\eta_{2MP^-,3MP^-}$

values (1.9 and 1.8, respectively) much larger than three-dimensional MEL zeolites (1.15), in spite of their similar apertures (0.51, 0.51, and 0.52 nm, respectively [23]). The stronger sieving effects of one-dimensional structures are well-known and assigned to “single-file diffusion” processes that impede molecular traffic much more severely than in more highly-connected voids [12–14,38–40]. The same trends are observed for  $\eta_{2MH^-,3MH^-}$  values as for  $\eta_{2MP^-,3MP^-}$  values but with larger magnitudes, reflecting the larger size of the isoheptenes compared to isohexenes.

These trends and their mechanistic assessments indicate that high selectivities to 2-methyl isomers as voids structures restrict molecular diffusion reflect the faster diffusion of these isoalkenes related to other alkene isomers, including those with branches farther from the terminal carbon atoms. Such specificity is attained even though 2-methyl and 3-methyl alkenes equilibrate rapidly within zeolite crystallites, because intracrystalline regions with small apertures, especially when composed of one-dimensional channels, discriminate against the egress of the slower diffusing 3-methyl isomers. Such sieving effects become less evident as void structures allow faster diffusion of both methyl isomers by increases in aperture size or dimensionality. These conclusions, supported by assessments of selectivities as  $NH_3$  desorbs and intracrystalline product gradients become more severe and by reaction-transport descriptions of selectivity, cast significant concerns over visually attractive but inaccurate heuristics that assign such preference for terminal methyl groups to the exclusive access to protons at the pore mouth by the linear alkene reactants. Such consequences of intracrystalline product concentration gradients for selectivity are, in fact, a direct consequence of the shape selective properties that make zeolites so ubiquitous in practice. Diffusion-enhanced secondary reactions become most evident for linear hydrocarbon reactants because their primary products are more reactive and diffuse more slowly than the linear alkene reactants. Their practical consequences for selectivity have been inaccurately interpreted in most cases as the effects of acid strength or transition state confinement on single-sojourn reaction events. In fact, they merely reflect fast secondary reactions that occur before products can be detected in the fluid phase. The same voids of molecular dimensions that stabilize transition states and sieve reactants and products based on diffusivities bring forth inherent obstacles to our direct observation of primary and secondary products, unless we intentionally seek to detect them using the methods described herein and through the use of materials with different proton densities and characteristic diffusion times and of reaction-transport formalisms designed to describe their consequences for reactivity and selectivity.

### 3.2.2. Undulations in medium-pore zeolites and their role in creating local environments that favor $\beta$ -scission of highly branched alkenes

This section describes and interprets the effects of intracrystalline gradients of the product 2,4-dimethylalkenes on  $\beta$ -scission selectivity using gradual  $NH_3$  desorption methods and the concept of local undulations [7,15]. These local undulations are created by the intersections of 10-MR channels in three-dimensional zeolites and are not present within one-dimensional structures. They provide local environments that favor the formation of the highly-branched isomers required for  $\beta$ -scission but simultaneously restrict their egress, thus increasing their local residence times. These local effects, prevalent at the scale of each intersection, represent the rigorous analog, conceptually and with respect to their consequences for selectivity, of product gradients at the crystallite length scale but without the benefits of continuum reaction-diffusion models, which become inappropriate to describe regions of molecular dimensions. The absence of undulations in one-dimensional channels lead to the low  $\beta$ -scission selectivities typical of MTT and TON zeolites; this is the performance characteristic

that, along with the terminal methyl isomer selectivity, makes these types of structures the most attractive acid catalysts in commercial practice for isomerization of linear paraffin for improving the flow properties of fuels and lubestocks.

The data in Fig. 6 show  $\beta$ -scission selectivities (reported on a carbon basis; Eq. (5)) on SVR, MTT, and TON (Fig. 6b–d, respectively; MTT-1 and TON-1 chosen to represent MTT and TON frameworks) as  $\text{NH}_3$  desorbs. The corresponding data for MEL and MFI are included in the Supporting Information (Section S3) and show trends similar to those for SVR. These  $\beta$ -scission selectivities increase as  $\text{NH}_3$  desorbs and  $\chi(t)$  increases; the resulting increases in proton densities ( $\rho_{\text{H}^+}$ ) and  $\phi_{\text{DMP}}$  values (Eq. (13), for dimethylpentenes) lead to stronger intracrystalline dimethylpentene gradients, thus enhancing their  $\beta$ -scission reaction before their hydrogenation at the external metal function. These  $\beta$ -scission selectivities should approach zero at initial times during titrant desorption ( $\chi(t) \rightarrow 0$ ) for all frameworks, because intracrystalline gradients must become negligible in this asymptotic limit. These single-sojourn selectivities reflect those of primary events and are observed under conditions of strict kinetic control (e.g., for FAU; Fig. 6a); they are indeed zero even on one-dimensional medium-pore (10-MR) MTT and TON frameworks (Fig. 6c and 6d, respectively).

In sharp contrast, these extrapolated  $\beta$ -scission selectivities are not zero on SVR, MFI, and MEL (0.08, 0.10, 0.15, respectively), indicative of significant  $\beta$ -scission reactions even as proton densities approach zero and as gradients at the crystallite length scale must become kinetically inconsequential. SVR, MFI, and MEL are undulating three-dimensional 10-MR frameworks, in which channel intersections create cage-like structures that accommodate transition states for the formation of highly-branched alkenes but restrict their egress, which becomes much more facile as they form smaller and less reactive fragments via  $\beta$ -scission. These local effects are insensitive to Thiele moduli and proton densities, which influence gradients at the crystallite length scale where continuum reaction-diffusion models can be applied. Such “single-cage” diffusional effects are also evident for primary  $\beta$ -scission reactions of 2,4-dimethylpentane extrapolated to zero  $\chi(t)$  [7] and become more evident as the “severity” of the undulations becomes more pronounced; for example, the extrapolated  $\beta$ -scission selectivity for 2,4-dimethylpentane reactants for SVR was 0.07, while that for MEL was 0.19.

A metric of the magnitude of these undulations was previously defined to describe “single-cage” scission events during alkene oligomerization [15]. This undulation factor ( $\Omega$ ) is defined as the ratio of the aperture diameter (pore-limiting diameter,  $d_{\text{PL}}$ ) to the intersection diameter (diameter of the largest contained sphere,  $d_{\text{LC}}$ ) for each framework:

$$\Omega = d_{\text{PL}}/d_{\text{LC}} \quad (17)$$

Structures with greater undulations have  $\Omega$  values smaller than unity, while the straight channels of one-dimensional zeolites lack undulations and are characterized by a  $\Omega$  value of unity.

Fig. 8 shows  $\beta$ -scission selectivities (as  $\chi(t) \rightarrow 0$ ) on 10-MR zeolites with different  $\Omega$  values. These selectivities are zero for MTT and TON, but they increase monotonically as  $\Omega$  decreases as a result of the channel intersections in three-dimensional frameworks. These single-cage events reflect multiple “collisions” of a molecule with an acid site present within a single cage before egressing from each local undulation. One-dimensional channels lack any consequential undulations, thus avoiding the single-cage effects that favor  $\beta$ -scission of dimethylpentenes retained within intersections in three-dimensional channel networks. The uniquely low  $\beta$ -scission selectivities that make MTT and TON zeolites attractive in practice arise from the absence of substantial undulations within these frameworks.

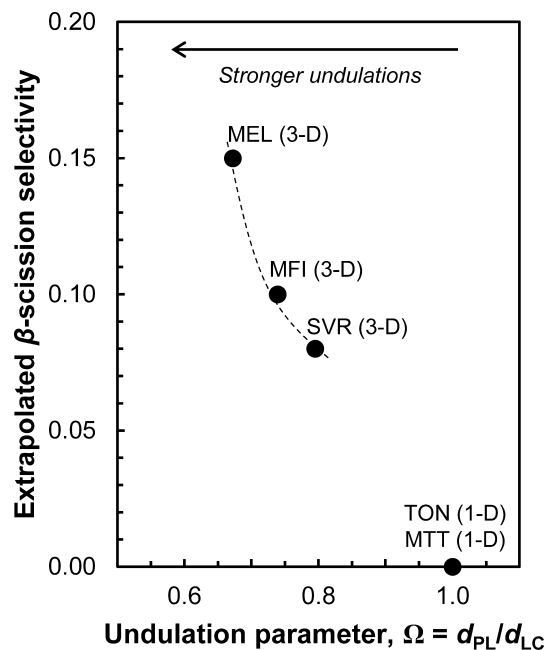


Fig. 8.  $\beta$ -Scission selectivities, extrapolated to zero accessible protons during  $\text{NH}_3$  desorption, on each 10-MR zeolite as a function of the undulation parameter,  $\Omega$  (Eq. (17) of the main text), of the aluminosilicate. The dashed line represents a guide for the eye.

The high selectivity to alkane products with terminal methyl branches and the low  $\beta$ -scission selectivity of MTT and TON acid zeolites in bifunctional hydroisomerization have been historically interpreted as the consequence of “pore-mouth catalysis” [8–11], a heuristic concept without firm theoretical basis and inconsistent with the diffusivities of such materials and with the data and reaction-diffusion models reported here. These catalytic features have been instrumental in the broad deployment of one-dimensional medium-pore zeolites in the practice of isomerization and oligomerization catalysis; they are the consequences of strong intracrystalline concentration gradients of isoalkenes, combined with the substantial absence of local undulations in these one-dimensional 10-MR zeolites. Such conclusions illustrate once again the inextricable connections between the confining properties and the diffusional restrictions imposed by crystalline structures with voids of molecular dimensions and their strong and, as we show here, now predictable consequences for reactivity and selectivity.

#### 4. Conclusions

n-Heptane and n-hexane isomerization reaction rates and selectivities were measured on physical mixtures of Pt/SiO<sub>2</sub> and mesoporous aluminosilicates (Al-MCM-41) or zeolites (FAU, SFH, BEA, MEL, MFI, SVR, MTT, TON). Linear heptenes and hexenes both exhibited kinetically-relevant intracrystalline concentration gradients in MTT and TON samples that varied in their proton densities and in their diffusion times for n-pentane, an accurate surrogate for crystallite size. Such concentration gradients implicate intrapore and not merely external acid sites as kinetically-relevant for isomerization.

Product isoalkenes are more reactive and have smaller diffusivities than their linear reactant counterparts, resulting in their more severe intracrystalline concentration gradients in MTT and TON. In contrast, on mesoporous Al-MCM-41, the ratio of 2-methyl to 3-methyl hexane isomers approaches equilibrium values for alkanes with increasing bed residence times, even at very low conversions,

indicating the absence of intracrystalline isoalkene concentration gradients. Similar findings are observed for large pore zeolites (FAU, SFH, and BEA), which exhibit weak intracrystalline gradients of methylhexanes that allow their full equilibration with alkane analogs; stronger gradients are observed for dimethylpentanes, as a result of their greater reactivity and smaller diffusivity than their less-branched counterparts, resulting in an increase in  $\beta$ -scission selectivity as  $\text{NH}_3$  titrants desorb.

Zeolitic acids characterized by 10-membered rings (MFI, MEL, SVR, MTT, TON), in contrast, exhibit strong intracrystalline gradients of all isoalkene products, which lead to 2-methyl to 3-methyl isomer ratios that reflect local equilibration of their isoalkene regioisomers (instead of isoalkanes) within the acid domains but also their respective intracrystalline diffusivities. As a result, isomer ratios remain constant as  $\text{NH}_3$  desorbs and intracrystalline proton densities increase, but also with changes in bed residence times.

2-Methyl to 3-methyl isomer ratios are larger (up to five-fold) on 10-MR zeolites than those predicted from isoalkene equilibration; these ratios increase as the aperture size and 10-MR channel connectivity decrease. The aperture size and the channel connectivity (1-D vs. 3-D) strongly influence diffusivities for guest molecules of a given backbone length and location of methyl substituents, with terminal methyl isomers diffusing faster than those with internal or multiple methyl groups. The ratio of 2-methyl to 3-methyl isomers formed from n-hexane also increases with as channel size and connectivity decrease, but less strongly than for n-heptane reactants, because intracrystalline gradients are less severe for the less reactive and faster-diffusing smaller chains.

The connectivity of 10-MR channels also determines the extent of secondary  $\beta$ -scission product formation. The intersecting channels in MFI, MEL, and SVR form larger voids with smaller interconnecting apertures; the undulations prevalent in these cage-window structures allow the facile local formation of bulkier dimethylpentene isomers, the exclusive precursors to  $\beta$ -scission, while also hindering their egress. These local diffusional constraints lead to non-zero  $\beta$ -scission selectivities, even when extrapolated to zero intracrystalline proton densities; these asymptotic selectivities reflect diffusional enhancements of secondary reactions at the local scale of these undulations, which become more evident as the severity of these undulations increases. In contrast, the absence of undulations in the one-dimensional channels of MTT and TON cannot locally form products larger than the apertures through which they must egress, the essential requirement for low  $\beta$ -scission selectivities.

We have demonstrated here that the high selectivity to single-branched alkanes with terminal methyl groups and the low  $\beta$ -scission selectivities iconic of MTT and TON zeolites arise not because of “pore-mouth catalysis” or other convenient heuristics but instead merely reflect the presence of intracrystalline gradients of product alkenes within non-undulating channels. Such a product distribution, desirable for use in fuels and lubestocks, is the result of the intimate entanglement between diffusive and reactive properties afforded by the small pores of zeolite materials.

## Acknowledgments

The authors acknowledge the financial support of the Chevron Energy Technology Company;  $R^2/D_{\text{HP}}$  measurements and analysis by Zhichen (Jane) Shi (Univ. of Minnesota, Twin Cities); and technical discussions with Dr. William Knaeble (Univ. of California, Berkeley) and Prof. Michele Sarazen (Princeton Univ.). G.N. acknowledges a Chevron Fellowship granted in support of this research.

## Declaration of Competing Interest

The authors declare the following competing financial interest (s):

- (1) The funding for this research came from Chevron Energy Technology Co. and
- (2) Stacey I. Zones is an employee of this company and, more generally, also a stockholder of Chevron Corp.

## Appendix A. Supplementary material

Supplementary data to this article can be found online at <https://doi.org/10.1016/j.jcat.2019.07.022>.

## References

- [1] S.J. Miller, Process for Making Middle Distillates Using a Silicoaluminophosphate Molecular Sieve, US4859312A, 1987.
- [2] S.J. Miller, A.J. Dahlberg, K.R. Krishna, R.R. Krug, Process for Producing a Highly Paraffinic Diesel Fuel Having a High Iso-paraffin to Normal Paraffin Mole Ratio, (2004) US6723889B2.
- [3] P.B. Weisz, Polyfunctional heterogeneous catalysis, *Adv. Catal.* 13 (1962) 137–190, [https://doi.org/10.1016/S0360-0564\(08\)60287-4](https://doi.org/10.1016/S0360-0564(08)60287-4).
- [4] H.L. Coonradt, W.E. Garwood, Mechanism of Hydrocracking. Reactions of Paraffins and Olefins, *Ind. Eng. Chem. Proc. Des. Dev.* 3 (1) (1964) 38–45, <https://doi.org/10.1021/i260009a010>.
- [5] G. Noh, Z. Shi, S.I. Zones, E. Iglesia, Isomerization and  $\beta$ -scission reactions of alkanes on bifunctional metal-acid catalysts: consequences of confinement and diffusional constraints on reactivity and selectivity, *J. Catal.* 368 (2018) 389–410, <https://doi.org/10.1016/j.jcat.2018.03.033>.
- [6] W. Knaeble, E. Iglesia, Acid strength and metal-acid proximity effects on methylcyclohexane ring contraction turnover rates and selectivities, *J. Catal.* 344 (2016) 817–830, <https://doi.org/10.1016/j.jcat.2016.08.007>.
- [7] G. Noh, S.I. Zones, E. Iglesia, Consequences of acid strength and diffusional constraints for alkane isomerization and  $\beta$ -scission turnover rates and selectivities on bifunctional metal-acid catalysts, *J. Phys. Chem. C* 122 (2018) 25475–25497, <https://doi.org/10.1021/acs.jpcc.8b08460>.
- [8] C.S. Laxmi Narasimhan, J.W. Thybaut, G.B. Marin, J.A. Martens, J.F. Denayer, G. V. Baron, Pore mouth physisorption of alkanes on ZSM-22: Estimation of physisorption enthalpies and entropies by additivity method, *J. Catal.* 218 (2003) 135–147, [https://doi.org/10.1016/S0021-9517\(03\)00069-1](https://doi.org/10.1016/S0021-9517(03)00069-1).
- [9] J.A. Martens, G. Vanbutsele, P.A. Jacobs, J. Denayer, R. Ocaoglu, G. Baron, J.A. Muñoz Arroyo, J. Thybaut, G.B. Marin, Evidences for pore mouth and key-lock catalysis in hydroisomerization of long n-alkanes over 10-ring tubular pore bifunctional zeolites, *Catal. Today* 65 (2001) 111–116, [https://doi.org/10.1016/S0920-5861\(00\)00577-0](https://doi.org/10.1016/S0920-5861(00)00577-0).
- [10] W. Souverijns, J.A. Martens, G.F. Froment, P.A. Jacobs, Hydrocracking of isoheptadecanes on Pt/H-ZSM-22: An example of pore mouth catalysis, *J. Catal.* 174 (1998) 177–184, <https://doi.org/10.1006/jcat.1998.1959>.
- [11] A. van de Runstraat, J.A. Kamp, P.J. Stobbeaer, J. van Grondelle, S. Krijnen, R.A. van Santen, Kinetics of hydro-isomerization of n-hexane over platinum containing zeolites, *J. Catal.* 171 (1997) 77–84, <https://doi.org/10.1006/jcat.1997.1779>.
- [12] Q.H. Wei, C. Bechinger, P. Leiderer, Single-file diffusion of colloids in one-dimensional channels, *Science* 287 (2000) 625–627, <https://doi.org/10.1126/science.287.5453.625>.
- [13] J. Kärger, M. Petzold, H. Pfeifer, S. Ernst, J. Weitkamp, Single-file diffusion and reaction in zeolites, *J. Catal.* 136 (1992) 283–299, [https://doi.org/10.1016/0021-9517\(92\)90062-M](https://doi.org/10.1016/0021-9517(92)90062-M).
- [14] K. Hahn, J. Kärger, Deviations from the normal time regime of single-file diffusion, *J. Phys. Chem. B* 102 (1998) 5766–5771, <https://doi.org/10.1021/jp981039h>.
- [15] M.L. Sarazen, E. Dorskocil, E. Iglesia, Effects of void environment and acid strength on alkene oligomerization selectivity, *ACS Catal.* 6 (2016) 7059–7070, <https://doi.org/10.1021/acscatal.6b02128>.
- [16] A.J. Jones, S.I. Zones, E. Iglesia, Implications of transition state confinement within small voids for acid catalysis, *J. Phys. Chem. C* 118 (2014) 17787–17800, <https://doi.org/10.1021/jp5050095>.
- [17] G.W. Skeels, D.W. Breck, Silicon substituted Y zeolite composition LZ-210, 4711770A, 1987.
- [18] S.I. Zones, Synthesis of pentasil zeolites from sodium silicate solutions in the presence of quaternary imidazole compounds, *Zeolites* 9 (1989) 458–467, [https://doi.org/10.1016/0144-2449\(89\)90039-0](https://doi.org/10.1016/0144-2449(89)90039-0).
- [19] S.I. Zones, B. Lee, L.-T. Yuen, T.M. Davis, J.N. Ziemer, A. Ojo, Method for Preparing Small Crystal SSZ-32, US 8,545,805 B2, 2013.
- [20] R.A. Alberty, C.A. Gehrig, Standard chemical thermodynamic properties of alkane isomer groups, *J. Phys. Chem. Ref. Data* 13 (1984) 1173–1197, <https://doi.org/10.1063/1.555726>.

- [21] G.A. Olah, Stable carbocations. CXVIII. General concept and structure of carbocations based on differentiation of trivalent (classical) carbenium ions from three-center bound penta- of tetracoordinated (nonclassical) carbonium ions. Role of carbocations in electrophilic substitution, *J. Am. Chem. Soc.* 94 (1972) 808–820, <https://doi.org/10.1021/ja00758a020>.
- [22] W. Knaeble, R.T. Carr, E. Iglesia, Mechanistic interpretation of the effects of acid strength on alkane isomerization turnover rates and selectivity, *J. Catal.* 319 (2014) 283–296, <https://doi.org/10.1016/j.jcat.2014.09.005>.
- [23] C. Baerlocher, L. McCusker, Database of Zeolite Structures, (n.d.). <<http://www.iza-structure.org/databases/>>.
- [24] R.A. Alberty, C.A. Gehrig, Standard chemical thermodynamic properties of alkene isomer groups, *J. Phys. Chem. Ref. Data.* 14 (1985) 803, <https://doi.org/10.1063/1.555737>.
- [25] A.J. Jones, E. Iglesia, The strength of Brønsted acid sites in microporous aluminosilicates, *ACS Catal.* 5 (2015) 5741–5755, <https://doi.org/10.1021/acscatal.5b01133>.
- [26] M. Rybicki, J. Sauer, Acid strength of zeolitic Brønsted sites—Dependence on dielectric properties, *Catal. Today.* (2018), <https://doi.org/10.1016/j.cattod.2018.04.031>.
- [27] E.W. Thiele, Relation between catalytic activity and size of particle, *Ind. Eng. Chem.* 31 (1939) 916–920, <https://doi.org/10.1021/ie50355a027>.
- [28] H.S. Fogler, *Elements of chemical reaction engineering*, 4th ed., Prentice Hall, 2005.
- [29] K.B. Bischoff, Effectiveness factors for general reaction rate forms, *AIChE J.* 11 (1965) 351–355, <https://doi.org/10.1002/aic.690110229>.
- [30] J. Xiao, J. Wei, Diffusion mechanism of hydrocarbons in zeolites—I. Theory, *Chem. Eng. Sci.* 47 (1992) 1123–1141, [https://doi.org/10.1016/0009-2509\(92\)80236-6](https://doi.org/10.1016/0009-2509(92)80236-6).
- [31] L. Karwacki, M.H.F. Kox, D.A. Matthijs de Winter, M.R. Drury, J.D. Meeldijk, E. Stavitski, W. Schmidt, M. Mertens, P. Cubillas, N. John, A. Chan, N. Kahn, S.R. Bare, M. Anderson, J. Kornatowski, B.M. Weckhuysen, Morphology-dependent zeolite intergrowth structures leading to distinct internal and outer-surface molecular diffusion barriers, *Nat. Mater.* 8 (2009) 959–965, <https://doi.org/10.1038/nmat2530>.
- [32] E.P.L. Hunter, S.G. Lias, Evaluated gas phase basicities and proton affinities of molecules: an update, *J. Phys. Chem. Ref. Data.* 27 (1998) 413–656, <https://doi.org/10.1063/1.556018>.
- [33] S. Herrmann, E. Iglesia, Elementary steps in acetone condensation reactions catalyzed by aluminosilicates with diverse void structures, *J. Catal.* 346 (2017) 134–153, <https://doi.org/10.1016/j.jcat.2016.12.011>.
- [34] M.L. Sarazen, E. Iglesia, Effects of charge, size, and shape of transition states, bound intermediates, and confining voids in reactions of alkenes on solid acids, *ChemCatChem.* 10 (2018) 4028–4037, <https://doi.org/10.1002/cctc.201800401>.
- [35] S. Calero, M. Schenk, D. Dubbeldam, T.L.M. Maesen, B. Smit, The selectivity of n-hexane hydroconversion on MOR-, MAZ-, and FAU-type zeolites, *J. Catal.* 228 (2004) 121–129, <https://doi.org/10.1016/j.jcat.2004.08.019>.
- [36] J. Xiao, J. Wei, Diffusion mechanism of hydrocarbons in zeolites-II. Analysis of experimental observations, *Chem. Eng. Sci.* 47 (1992) 1143–1159, [https://doi.org/10.1016/0009-2509\(92\)80237-7](https://doi.org/10.1016/0009-2509(92)80237-7).
- [37] C.L. Cavalcante, D.M. Ruthven, Adsorption of branched and cyclic paraffins in silicalite. 2. Kinetics, *Ind. Eng. Chem. Res.* 34 (1995) 185–191, <https://doi.org/10.1021/ie00040a018>.
- [38] J. Kärger, D.M. Ruthven, D.N. Theodorou, *Diffusion in nanoporous materials*, Wiley-VCH, Weinheim Germany, 2012, <https://doi.org/10.1002/9783527651276.ch18>.
- [39] K. Hahn, J. Kärger, V. Kukla, Single-file diffusion observation, *Phys. Rev. Lett.* 76 (1996) 2762–2765, <https://doi.org/10.1103/PhysRevLett.76.2762>.
- [40] V. Gupta, S.S. Nivarthi, A.V. McCormick, H. Ted Davis, Evidence for single file diffusion of ethane in the molecular sieve AIP04-5, *Chem. Phys. Lett.* 247 (1995) 596–600, [https://doi.org/10.1016/S0009-2614\(95\)01246-X](https://doi.org/10.1016/S0009-2614(95)01246-X).